


# JGR Solid Earth

## RESEARCH ARTICLE

10.1029/2023JB027549

# A Comprehensive Stress Drop Map From Trench to Depth in the Northern Chilean Subduction Zone

J. Folesky<sup>1</sup> , C. N. Pennington<sup>2</sup>, J. Kummerow<sup>1</sup>, and L. J. Hofman<sup>1</sup>

<sup>1</sup>Department of Geophysics, Freie Universität Berlin, Berlin, Germany, <sup>2</sup>Lawrence Livermore National Laboratory, Livermore, CA, USA

### Key Points:

- A comprehensive stress drop distribution with more than 51,000 stress drop estimates for the Northern Chilean Subduction Zone is computed
- Systematic stress drop variations between upper plate, interface and intermediate depth seismicity are revealed
- Reliability and comparability of results are increased by using two methods, the spectral ratio and the spectral decomposition approach

### Supporting Information:

Supporting Information may be found in the online version of this article.

### Correspondence to:

J. Folesky,  
[jonas.folesky@geophysik.fu-berlin.de](mailto:jonas.folesky@geophysik.fu-berlin.de)

### Citation:

Folesky, J., Pennington, C. N., Kummerow, J., & Hofman, L. J. (2024). A comprehensive stress drop map from trench to depth in the northern Chilean subduction zone. *Journal of Geophysical Research: Solid Earth*, 129, e2023JB027549. <https://doi.org/10.1029/2023JB027549>

Received 27 JUL 2023  
Accepted 10 DEC 2023

### Author Contributions:

**Conceptualization:** J. Folesky  
**Data curation:** J. Folesky, J. Kummerow, L. J. Hofman  
**Formal analysis:** J. Folesky  
**Funding acquisition:** J. Folesky  
**Investigation:** J. Folesky, L. J. Hofman  
**Methodology:** J. Folesky, C. N. Pennington, L. J. Hofman  
**Project Administration:** J. Folesky  
**Supervision:** J. Folesky  
**Validation:** J. Folesky  
**Visualization:** J. Folesky

© 2024 The Authors.

This is an open access article under the terms of the [Creative Commons Attribution-NonCommercial License](https://creativecommons.org/licenses/by-nc/4.0/), which permits use, distribution and reproduction in any medium, provided the original work is properly cited and is not used for commercial purposes.

**Abstract** We compute stress drops for earthquakes in Northern Chile recorded between 2007 and 2021. By applying two analysis techniques, (a) the spectral ratio (SR) method and (b) the spectral decomposition (SDC) method, a stress drop map for the subduction zone consisting of 51,510 stress drop values is produced. We build an extended set of empirical Green's functions (EGF) for the SR method by systematic template matching. Outputs are used to compare with results from the SDC approach, where we apply cell-wise obtained global EGF's to compensate for the structural heterogeneity of the subduction zone. We find a good consistency of results of the two methods. The increased spatial coverage and quantity of stress drop estimates from the SDC method facilitate a consistent stress drop mapping of the different seismotectonic domains. Albeit only small differences of median stress drop, strike-perpendicular depth sections clearly reveal systematic variations, with earthquakes at different seismotectonic locations exhibiting distinct values. In particular, interface seismicity is characterized by the lowest observed median value, whereas upper plate earthquakes show noticeably higher stress drop values. Intermediate depth earthquakes show comparatively high average stress drop and a rather strong depth-dependent increase of median stress drop. Additionally, we observe spatio-temporal variability of stress drops related to the occurrence of the two megathrust earthquakes in the study region. The presented study is the first coherent large scale 3D stress drop mapping of the Northern Chilean subduction zone. It provides an important component for further detailed analysis of the physics of earthquake ruptures.

**Plain Language Summary** Stress drop is the released stress on a fault during a seismic rupture. We compute stress drops for earthquakes in northern Chile recorded between 2007 and 2021. By applying two different analysis techniques, (a) the spectral ratio method and (b) the spectral decomposition method, a stress drop map for the subduction zone consisting of 51,510 stress drop values is produced. We find a good consistency of results of the two methods. The good spatial coverage and quantity of stress drop estimates allow a consistent stress drop mapping of the seismically active domains. Although differences of median stress drops are relatively small, the depth section clearly reveals systematic variations, with earthquakes of different classes. In particular, interface seismicity is characterized by the low median values, whereas upper plate earthquakes show noticeably higher stress drops. Intermediate depth earthquakes show comparatively high average stress drop and depth-dependence. Additionally, we observe variability of stress drops related to the occurrence of the two megathrust earthquakes in the study region. The here presented study is the first large scale 3D stress drop mapping of the Northern Chilean subduction zone. It provides an important component for further analysis of the physics of earthquake ruptures.

## 1. Introduction

Stress drop is the seismological parameter that relates seismic moment and average slip to the rupture dimension. It characterizes the earthquake source, and its spatial-temporal distribution and possible correlation with other properties such as earthquake depth, mechanism or stress state may contribute to a better physical understanding of earthquakes.

A number of studies report scale-invariance or self-similarity, that is, a fundamentally constant average stress drop which is then used to obtain rupture size or average slip (e.g., Aki, 1967; Shaw, 2009). From detailed studies of individual events, however, it becomes increasingly clear that stress drops may actually be widely variable, usually ranging between about 0.1 and 100 MPa (e.g., Abercrombie, 1995; Allmann & Shearer, 2009; Bindi et al., 2020). Therefore, a possible scale-invariance over several magnitudes is debated. It is supported by some studies, for example, Abercrombie (1995); Shearer et al. (2006), and contested by others, for example, Prieto

**Writing – original draft:** J. Folesky, J. Kummerow

**Writing – review & editing:** J. Folesky, C. N. Pennington, J. Kummerow, L. J. Hofman

et al. (2013); Nishitsuji and Mori (2014); Trugman and Shearer (2017) or Bindi et al. (2020), who observe a dependence of stress drop on seismic moment. It has also been pointed out that estimates of the stress drop value strongly depend on the analysis method (Neely et al., 2020; Shearer et al., 2019), the model assumptions and the parameter choices (Ji et al., 2022; Kaneko & Shearer, 2014, 2015), thus complicating a comparison of results from different studies.

Stress drop values of large to megathrust earthquakes have been analyzed in several global studies (e.g., Allmann & Shearer, 2009; Ye et al., 2016), and crustal earthquakes, both of tectonic and induced origin, have been studied intensively in the last years to infer dependencies on depth, mechanism, magnitude and more (e.g., Abercrombie, 1995; Abercrombie, 2014; Bindi et al., 2020; Chen & Abercrombie, 2020; Goertz-Allmann et al., 2011; Hardebeck & Aron, 2009; Shearer et al., 2006; Trugman & Shearer, 2017). Most studies, however, are limited to a highly focused target zone or a relatively small amount of earthquakes usually not exceeding a few tens or hundreds of events, and systematic stress drop studies in particular of entire subduction zones or at least major parts of them are very rare (Allmann & Shearer, 2009; Tian et al., 2022; Uchide et al., 2014). And yet, knowledge of the variability of stress drop across an entire subduction system, which includes conditions for earthquake generation that can vary widely both spatially and temporally within an earthquake cycle, is particularly valuable.

As mentioned above, an important precondition for this type of study is the consistent and careful processing of a large number of events (i.e., many thousands of events), and the Northern Chilean subduction zone with its high seismic activity and dense seismic monitoring provides an ideal setting.

In an earlier study, Folesky et al. (2021) implemented and verified a spectral ratio approach (SR) for stress drop estimation for the rupture and aftershock area of the 2014  $M_w$ 8.1 Iquique earthquake. Analyzing ~600 events, they identified an increase of stress drop with distance from the plate interface, no clear depth dependence and an increase of stress drop with seismic moment. Additionally, they described the spatio-temporal variation of stress drop in association with the Iquique event.

In this work, we expand the analysis to the greater subduction zone in Northern Chile, a region that has been continuously monitored since 2006 by the IPOC network (IPOC, 2006) accompanied by the permanent networks of the CSN (C,C1) and multiple temporary deployments. Based on these data the distributions of several geophysical parameters in this region such as focal mechanisms, stress orientation, fore-, and aftershock distributions, or inter-plate-locking have been studied intensively by various authors (e.g., Cesca et al., 2016; Fuenzalida et al., 2013; Hoffmann et al., 2018; Li et al., 2015; Ruiz et al., 2014; Schurr et al., 2012; Schurr et al., 2014). An earthquake catalog covering the time period from 2007 to 2014 by Sippl et al. (2018) has recently been updated and extended until 2021 (Sippl et al., 2023). The new version contains over 180,000 events for the time period from 2007 to 2021. Its uniform processing along with the long time period make it a great basis for a comprehensive stress drop mapping of an entire subduction zone. Additionally, it allows for the detailed study of possible regional variations of stress drop as well as time-dependent variations in connection with the occurrence of two megathrust earthquakes, the 2007  $M_w$ 7.7 Tocopilla earthquake and the 2014  $M_w$ 8.1 Iquique earthquake.

We apply two different methods for calculating the stress drop: (a) the spectral ratio method (SR) and (b) the spectral decomposition method (SDC). Spectral ratio approaches employ empirical Green's functions (EGFs) to eliminate path and site terms in the observed seismogram spectrum and to isolate the event source term (e.g., Hutchings & Viegas, 2012). While this makes them more robust against systematic errors introduced by over- or under-correcting for attenuation structures and radiation pattern, they require the existence of a suitable nearby EGF event which, in practice, is a rather strong limitation. To overcome this problem, we additionally use a second approach which has proven to be better suited for large data sets and which increases significantly the quantity and spatial coverage of stress drop values. The spectral decomposition method (e.g., Chen & Abercrombie, 2020; Pennington et al., 2021; Prieto et al., 2004; Shearer et al., 2006) implicates to first untangle path, site, and event terms of multiple earthquakes simultaneously and then produce an EGF-like correction term which can be applied to an event cell rather than just to single events. In this way, the number of stress drop estimates can be multiplied at the cost of a more general correction of the source medium response.

In this study, we use the two methods jointly, which allows exploiting the benefits of both of them, to mutually control results and to produce a database of tens of thousands of stress drop values. The resulting distribution covers all the different seismically active segments of the subduction zone, from shallow depths close to trench down to depths of about 180 km.

## 2. Catalog and Data

We extract the event origin times, P- and S- arrival time picks, event hypocenters and magnitudes from the catalog by Sippl et al. (2023), which is an updated version of Sippl et al. (2018). In the following, we will refer to the new catalog as the IPOC catalog. It comprises 182,847 double-difference relocated events which occurred in the time period from 2007 to 2021. For our stress drop study, we use waveforms of in total 23 seismic broadband stations of the Integrated Plate Boundary Observatory Chile (IPOC, 2006). The network extends in N-S direction from 17.6°S to 24.6°S, a trench-parallel length of about 700 km. The corresponding continuous three-component waveform data, sampled at 100 Hz, were downloaded from the EIDA web service of GFZ Potsdam (Bianchi et al., 2015). Based on event location, the authors assign a class to each event of the IPOC catalog, picking from the following options:

- UP** Upper plate seismicity, predominantly crustal events within the South American plate, but also some earthquakes in the uppermost mantle.
- P1** Seismicity at or very close to the plate interface.
- P2** A plate interface-parallel band of seismicity in the oceanic Nazca Plate.
- P3** A second, deeper interface-parallel band of seismicity below P2.
- ID** Intermediate depth seismicity (sometimes called IDE). This class comprises by far the largest amount of events (~116,000), and it extends from about 60 km down to 180 km depth.
- MI** Mining events from open pit mines at the surface.
- NN** Not classified events which are located at the less well constrained edges of the catalog region outside the network. The two biggest subgroups are offshore events and deep event in the east, respectively.

Figure 1 displays the seismicity distribution from the IPOC catalog in Northern Chile, color-coded by depth. It includes a West-East depth view of a catalog slice with coloring according to the event class (dashed box). For a more detailed description of the event classification, the reader is referred to Sippl et al. (2018).

Stable magnitude estimation is an important prerequisite for consistent stress drop estimates, as the moment is an integral parameter in the estimate. Event magnitudes in the IPOC catalog were computed using a technique by Münchmeyer et al. (2020), which applies location-dependent station corrections in order to stabilize the computation against possible reduced or variable station availability. When plotted against relative moments, derived from the low frequency displacement plateau, we find a 1:1 relation (Figure S1 in Supporting Information S1). Thus, we use them to compute seismic moments.

The spectral ratio technique strongly depends on the availability of suitable event pairs which are used as a target and empirical Green's function couple. In order to exploit the existing data set at its best, we first perform an exhaustive event search by template matching, which complements the IPOC catalog by finding additional, small magnitude EGF candidate events. Template matching uses the cross correlation function to detect waveforms in a continuous data set that resemble the predefined patterns (i.e., the template waveforms). It is commonly used in seismology to increase the number of mostly weak events missed in the original earthquake catalog. Event seismograms from the catalog serve as templates, and the resulting detections can be assumed to be closely located and to have similar mechanisms as the template events, if cross correlation values are sufficiently high. This method becomes computationally challenging with an increasing volume of continuous waveform data and a high number of template events in the initial catalog. To make the method feasible for our extensive data set, we applied our own GPU-based template matching code. For each event in the IPOC catalog, template waveforms were extracted for the three closest available stations using the vertical channel only. The minimum length of the template waveform is 15 s and increases with hypocentral distance to include both the P and S phases. Additionally, the data was downsampled to 25 Hz. We define potential pairs of target event and empirical Green's function (EGF) event, if the normalized cross correlation coefficient is at least 0.70 at minimum two stations, with template waveforms derived from the same master event. In this way, the originally ~180,000 templates produce 1,836,195 matches, providing a substantial extension of the number of EGF candidates compared to the initial catalog.

## 3. Methods

### 3.1. Source Model and Stress Drop

We compute the stress drop  $\Delta\sigma$  assuming the widely used circular source model by Eshelby (1957):

$$\Delta\sigma = \frac{7\pi\mu\bar{D}}{16r} = \frac{7M_0}{16r^3}, \quad (1)$$

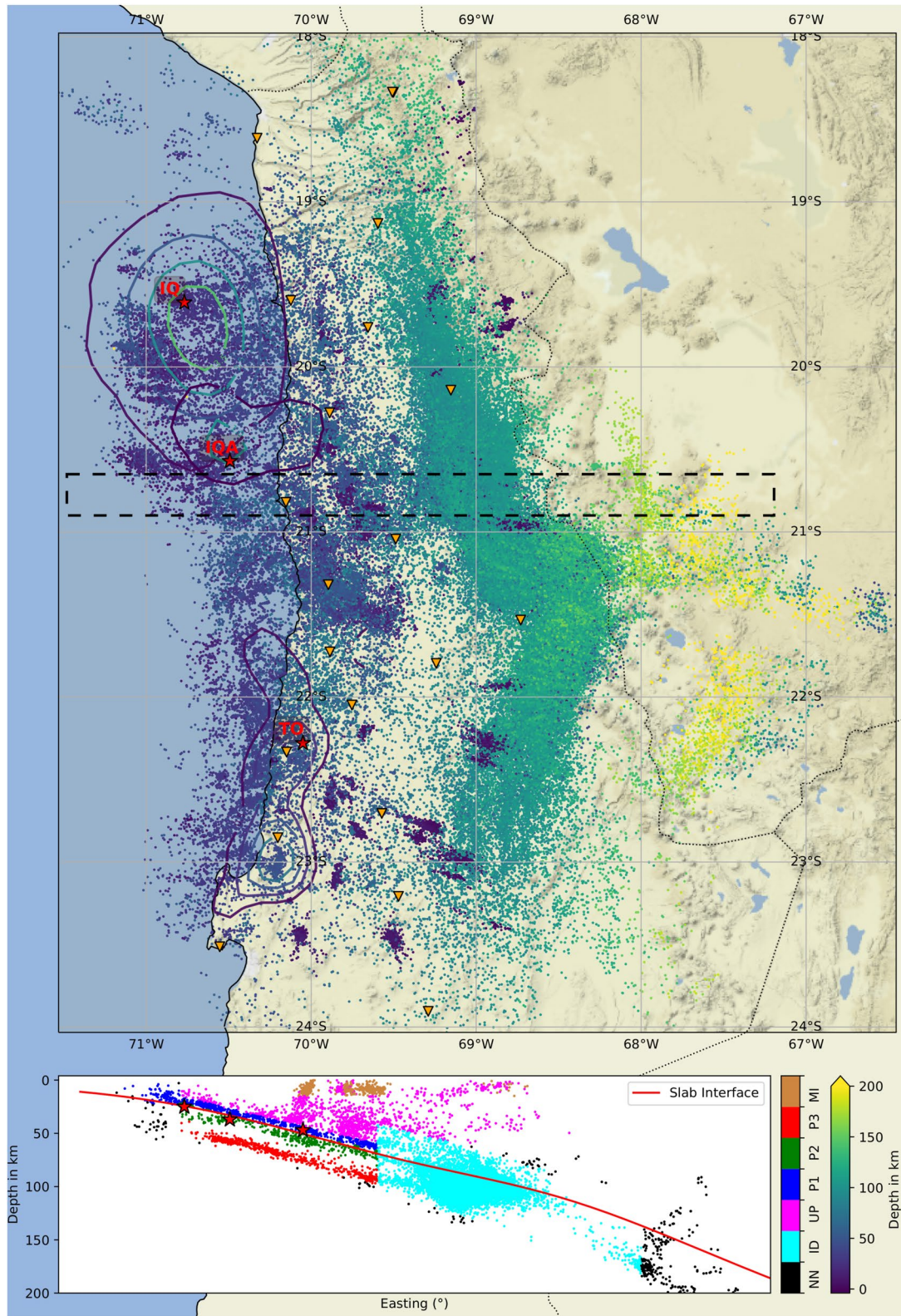


**Figure 1.** Seismicity from the IPOC catalog by Sippl et al. (2023). Color indicates event depth. Red stars are hypocenters of the  $M_w$ 8.1 2014 Iquique event (IQ), its largest  $M_w$ 7.6 aftershock (IQA), and the 2007  $M_w$ 7.7 Tocopilla event (TO). Their slip contours are taken from Schurr et al. (2012, 2014). Orange triangles show the location of the IPOC seismic stations. The bottom panel shows a depth view of selected events from the dashed box, color-coded by the associated event class, as explained in the text. The slab interface is taken from the model of Hayes et al. (2018).

where  $r$  is the approximate fault radius,  $\bar{D}$  is the average slip on the fault,  $\mu$  is the shear modulus, and  $M_0$  is the seismic moment. In general, slip and fault dimensions are not known, and the stress drop cannot be computed directly (Kanamori & Anderson, 1975). We therefore adopt the approach of Brune (1970), who proposed the following relation between source radius and spherically averaged corner frequency (see also Kaneko & Shearer, 2014, 2015; Madariaga, 1976):

$$f_c = k \frac{\beta}{r}, \quad (2)$$

with the shear wave velocity at the source,  $\beta$ , and a constant  $k$  that relates to the spherical average of the corner frequency for a specific theoretical source model. Combination of Equations 1 and 2 leads to the Brune type stress drop (Brune, 1970):

$$\Delta\sigma = \frac{7}{16} \left( \frac{f_c}{k\beta} \right)^3 M_0. \quad (3)$$

The seismic moment  $M_0$  is computed from the refined magnitudes of the IPOC catalog. We use the regional velocity model by Bloch et al. (2014) to compute event location-specific shear wave velocities. We use a  $k$ -value of  $k_p = 0.32$  for P-wave spectra, a standard value from Madariaga (1976), and we obtain  $k_s = 0.265$  by a least square fit of corner frequencies from both P and S phases for identical events, similar to Folesky et al. (2021). In practice,  $k_s$  is chosen such that P and S phase-based corner frequencies produce similar stress drop values. According to Kaneko and Shearer (2014) the here obtained  $k$ -values correspond to their model of a symmetrical circular rupture with a rupture velocity of  $v_r = 0.7\beta$ .

The corner frequency  $f_c$  is obtained by fitting a spectral model to the earthquake source spectrum. This is not recorded directly, and we only have the observed displacement spectrum  $d(f)$ , for which we can write

$$d(f) = e(f) \cdot p(f) \cdot s(f), \quad (4)$$

with the earthquake source spectrum,  $e(f)$ , the path response,  $p(f)$  and the site response,  $s(f)$ . The source spectrum can be expressed as

$$e(f) = \Omega_0 \frac{1}{(1 + (f/f_c)^n)^{1/\gamma}}, \quad (5)$$

where  $\Omega_0$  is proportional to the seismic moment,  $n$  is the high frequency falloff and  $\gamma$  is a constant which is commonly set to  $\gamma = 1$  for the Brune (1970) or  $\gamma = 2$  for the Boatwright (1980) spectral model, respectively.

Separating the terms in Equation 4 in order to apply the spectral model requires careful processing and may be achieved by using one of the following two methods.

### 3.2. Spectral Ratio Approach

For the spectral ratio approach, we use the processing scheme described in detail in Folesky et al. (2021), where a limited region around the 2014 Mw8.1 Iquique earthquake was already investigated.

The general idea of the spectral ratio method (SR) is to use for each target earthquake a smaller event with similar location and focal mechanism as an empirical Green's function (EGF) (Hutchings & Viegas, 2012). By spectral division between target and EGF seismograms the path and site terms which are assumed to be identical are removed (cf. Equation 4), leaving essentially the source term of the target event for frequencies below the corner frequency of the smaller event. The quotient now reads:

$$\frac{d_1(f)}{d_2(f)} \approx \frac{e_1(f)}{e_2(f)} = \frac{\Omega_{01}}{\Omega_{02}} \cdot \left[ \frac{1 + (f/f_{c2})^n}{1 + (f/f_{c1})^n} \right]^{1/\gamma}. \quad (6)$$

In practice, the similarity of the event locations is ensured by a required minimum cross correlation value between the waveforms of the two events at usually multiple stations. From our template matching results, described in Section 2, we select all templates with a catalog magnitude  $M \geq 2$  which produced matches having a cross correlation value of  $cc \geq 0.70$  at minimum 2 stations ( $n = 1,836,195$ ). If at least four picks are available, the

three-component waveform data are band-pass filtered (0.8–40 Hz) and sliced to maximum 6 and 10 s phase windows for P and S waves, respectively. A shorter S-P arrival time difference leads to shorter windows, accordingly. We require a SNR  $\geq 3$  in the frequency bands 1.5–5, 5–10, 10–15, 15–20, 20–25 Hz, for both template and EGF. Then, the spectral ratio is computed station-wise, and the quotient of the two Boatwright spectral models is fitted to the data. We require the median of the low frequency plateau to be higher than 5 to ensure sufficient difference of seismic moment between target and EGF, a necessity for resolving the corner frequency (Abercrombie, 2015). Next, the spectral ratios of all stations are stacked for robustness and resampled to achieve similar weights of low and high frequency content. The fit of the stack to the above Boatwright model quotient yields the corner frequency estimate of the target event. We show a data example of the procedure in Figure 2.

If the value of the corner frequency is within the interval 1–30 Hz, the stress drop is computed for this event. We obtain 25,994 P phase estimates and 36,121 S phase estimates which include multiple results for identical target events, originating from different EGF events. This enables us to estimate the statistical error of the corner frequency. Figure 3a illustrates the normalized differences to the median corner frequency for each event, where each data point is computed as  $\Delta f_{cij} = \frac{|\bar{f}_{ci} - f_{cij}|}{\bar{f}_{ci}}$ , for event  $i$ ,  $f_c$  estimate  $j$ , and event wise median corner frequency  $\bar{f}_{ci}$ . We obtain a standard deviation of 0.17, meaning that 50% of the estimates have a  $f_c$ -difference  $\leq 17\%$  to their family median.

Further details on the SR procedure, its limitations and error estimates are explained and discussed in Folesky et al. (2021).

### 3.3. Spectral Decomposition Approach

For the spectral decomposition approach (SDC), we use the decomposition procedure by Chen and Abercrombie (2020) as implemented in Pennington et al. (2021) and called SNSS (Stacking No assumption of Self-Similarity). The approach exploits the redundancy of existing event-station pairs to separate the displacement spectrum into event term, path term and site response (cf. Equation 4). A robust iterative stacking procedure as described in Shearer et al. (2006) is used to solve this over-determined problem, which should account for distance-dependent attenuation and site responses. The specific near-source attenuation, however, is assumed to be common for all event source paths, and therefore it needs to be estimated. For this, a so-called global empirical Green's function (gEGF), which is valid for the specific region, is computed. The gEGF can be used later in a similar way to the spectral ratio approach to compute the event-specific source time function properties such as the corner frequency. The construction of the gEGF is done as described in Chen and Abercrombie (2020) and Pennington et al. (2021). It consists of (a) a stacking step, where the phase spectra of all available events from the target region are stacked in 0.2 magnitude units, (b) a misfit computation between the lowest stack of those magnitude bins and different test values of corner frequency put into a spectral Brune model, (c) using the misfit as first gEGF and correction of the stacked spectra of all other magnitude bins, allowing for variable stress drop for each bin, (d) a fit of the now corrected spectra to obtain the overall misfit, (e) defining the final the correction function which produces the lowest misfit with each bin as the gEGF. This global empirical Green's function can then be used to correct all target events in the associated region, after which the individual corner frequency can be computed. A data example for a single event is shown in Figure 4.

The spectral decomposition method works best for a sufficiently high number of stacked spectra, that is, many events recorded on many stations in a confined region. The IPOC network consists of 23 stations, but due to the large spatial extent of the network, the weaker events are usually only recorded on a smaller subset of stations. Therefore, a relatively large amount of events is needed for the decomposition and computation of an appropriate gEGF. At the same time, strong variations of ray paths and attenuation are to be expected in a subduction zone. Hence, it makes sense to subdivide the volume into cells with a common gEGF, where the attenuation structure is assumed constant. We define a regular grid over our study region and divide it into cells of  $0.5^\circ \times 0.5^\circ \times 20$  km. For each cell to be processed, a minimum number of 100 catalog events of  $M \geq 1.8$  is required. The waveforms are band-pass filtered (0.8–40 Hz) and sliced into maximum 6 and 10 s phase windows for P and S waves, respectively, starting 0.1 s before the phase arrival and having shorter windows in case of shorter S-P arrival time differences. We only keep waveforms with an SNR  $\geq 3$  in the frequency bands 1–5, 5–20, and 20–40 Hz. Then, spectra are stacked in bins of 0.2 magnitude units. The bin that is used to compute the initial gEGF ( $1.8 \leq M < 2.0$ ) must contain at least 30 stacked spectra. After the spectral stacking, the result is checked for convergence by examining the misfit grid search results of the different test stress drop values. If a minimum is found within the grid search interval boundaries, the gEGF is used for this region. For all events with  $M \geq 2$  and a minimum of four valid spectra, the individual corner frequencies are computed by correcting the individual event term from the earlier decomposition with the gEGF.

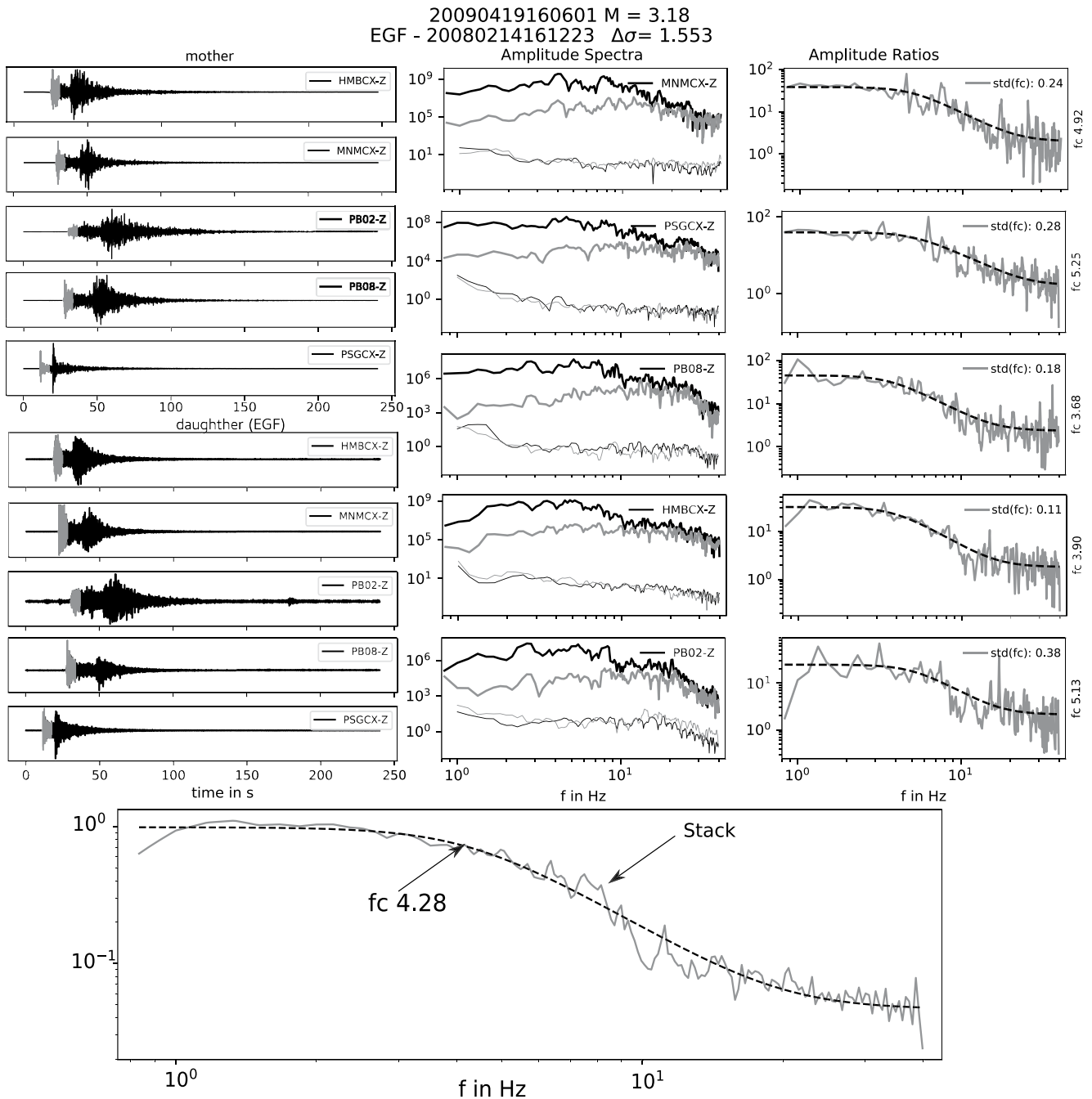


**Figure 2.** Spectral decomposition data example (event 20090419060601). Displacement waveforms for the mother event and the daughter event (EGF) are shown. The utilized phase window is highlighted in gray. The amplitude spectra of the mother event and its associated noise spectrum are shown in black, the spectra for daughter event and its noise in gray. The single station spectral ratios are fitted with a Boatwright model and std is the standard deviation for the  $f_c$ . The bottom panel shows the stack of all single station spectral ratios. A Boatwright spectral ratio model is fitted to the data with an optimal corner frequency estimate of 4.28 Hz. Note, that for a better view only z-components are plotted, while more were stacked. All components as well as more examples are shown in the supplement Figures S2–S9.

The resulting corner frequencies are required to lie between 1 and 30 Hz. To apply this procedure to the entire region of cataloged seismicity, the cells are shifted stepwise by  $0.25^\circ$  in horizontal and by 10 km in vertical direction. The step size is set to 50% of the cell width to ensure full overlap between cells.

We test the robustness of the multi-cell application of the spectral decomposition method by analyzing the variation of the gEGF with depth for a selected region and comparing it with a decomposition of the events from the same region treated as a single cell. We choose the location  $20.5^\circ\text{--}21.0^\circ \times 68.5^\circ\text{--}69.0^\circ$  and process six cells with

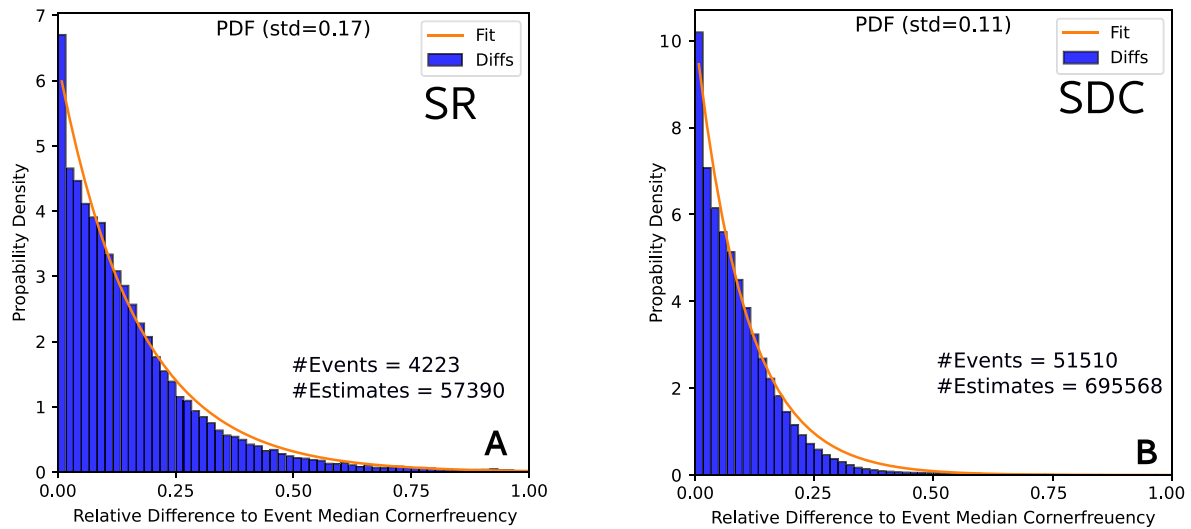


**Figure 3.** Normalized corner frequency variability from redundant measurements. For each mother event the corner frequency is computed as the median of all estimates from all measurements. (a) The SR technique produces redundant measurements based on multiple EGFs for the same mother event. (b) In the SDC method multiple stress drop estimates occur due to the cell wise computation of the gEGF. The normalized difference (see text) to the event wise median for both groups is fitted with an exponential decay distribution yielding standard distributions of 0.17 and 0.11 for SR and SDC corner frequencies, respectively.

varying top depths from 80 to 130 km. Figure 5a shows the corresponding gEGF of each cell, together with the single cell gEGF as a dashed line.

A higher value of a gEGF indicates a stronger attenuation correction for this frequency point in the source region. The correction decreases with depth (Figure 5a). Note that the gEGF only represents the spectral correction, which is not already captured in the path term ( $p$  in Equation 4). The single cell gEGF lies in the center of the ensemble of correction functions, representing some sort of average attenuation structure of the region. The corresponding median stress drop curve (Figure 5b) behaves accordingly: compared to the stress drop variation derived from the multi-cell gEGFs (black line), the resulting stress drop variations for the single cell (dashed line) appear under-corrected for deeper events and over-corrected for shallower events, while the variability of single cell stress drop appears smoother in general. We perform a similar test for a north-south multi-cell, crossing the entire catalog in Supporting Information S1 (Figure S10).

The tests demonstrate that the overall variation of stress drop remains similar, but the smaller scale attenuation heterogeneity is lost by using the single cell version. It also shows that the most populated cells dominate the gEGF. For our target area the great majority of cells include 100–1,000 events, while several cells have more than

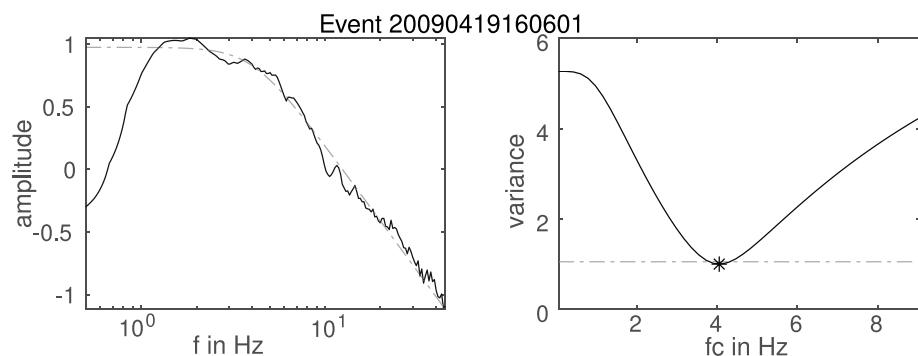


**Figure 4.** Spectral decomposition data example for event (20090419160601 same as in Figure 2). Boatwright's spectral model is fitted to the stack of all available gEGF corrected spectra for the event. The optimal corner frequency estimate (4.1 Hz) is obtained using the variance reduction method (Viegas et al., 2010). It is indicated by the star. The dashed line represents the 5% variance limit. More examples for SR and SDC single event results are shown in the supplement (Figure S8 and S9 in Supporting Information S1).



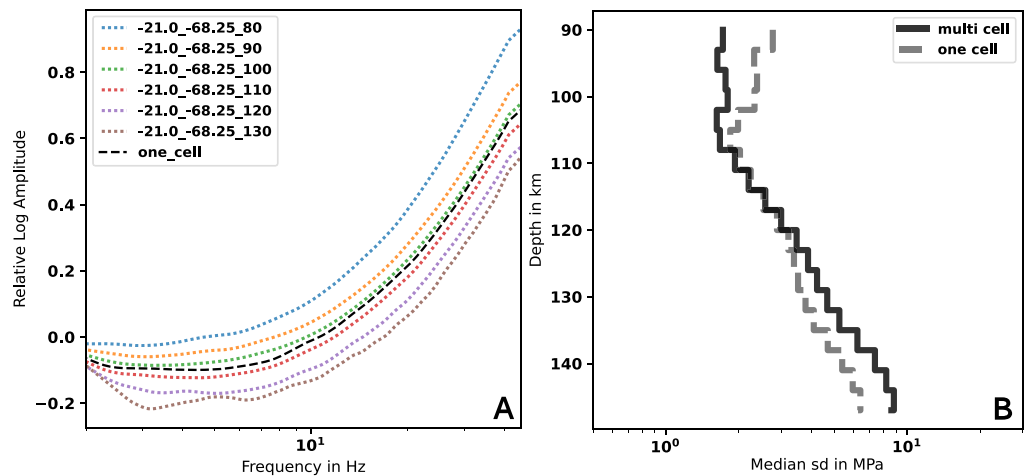


**Figure 5.** (a) Variation of gEGFs for six grid cells with changing depth. The black dashed line is the gEGF where all events from these cells are decomposed simultaneously in the processing. (b) The corresponding variation of median stress drop with depth for the multi-cell test and the single cell test. Albeit the similar curve shape, note the deviation at shallow depth, where the multi-cell gEGF have higher correction values (blue line in A) and the inverse behavior at greater depths.

5,000 (cf. Figure 11). These exclusively deep cells would dominate the gEGF of possible larger cells, and the characteristics of the shallower events would be lost.

To further test stability, we additionally computed results for a coarser grid with  $0.7^\circ \times 0.7^\circ$  cell size and a minimum event number of 400 in each cell. The stress drop distribution is slightly smoother compared to that obtained by using the smaller cells, but very similar in general. To illustrate the similarity we plot the spatial distribution, histogram and depth variability similar to Figures S6 and S7 in Supporting Information S1 (Figure S12).

Because of the utilized overlap between grid cells, many events have up to 16 independent stress drop estimates (8 for P, 8 for S wave) that are expected to vary slightly due to different gEGFs calculated for each cell. From the total number of estimates (695,568) and the total number of events (51,510) we obtain an average of about 14 stress drop estimates per event. The final stress drop value for each single event is computed from the median of all these estimates. Figure 3b shows that the average relative difference between the single corner frequency estimates to their respective family median is small (std = 11%). Hence, the consistency of corner frequency estimates between cells is high. This also confirms that the cell-wise gEGFs involve smooth and mostly subtle rather than abrupt changes of corner frequency. Hence, we do not expect that cell bounds strongly influence the obtained stress drop distribution.

From the performed tests, we conclude that the cell-wise application of the decomposition technique works reasonably well in the given setup. In addition, the following section will show the principal similarity between results from our implementations of the SDC approach and the SR method.

## 4. Results

### 4.1. Comparison of SR and SDC Results

The spectral decomposition method produces stress drop estimates for 51,510 events which are an almost complete superset of the 4,223 stress drop solutions from the spectral ratio method, meaning that any event that has an SR based stress drop estimate also has an SDC based stress drop estimate. Figure 6 displays map views of stress drop values and their corresponding histograms separately for both methods. Figure 7 displays the overall median stress drop variation against depth for both methods. The evident consistency demonstrates that, qualitatively, the results from both methods are very similar.

In Figure 7c the similarity is quantified as a cross plot of corner frequencies obtained for common events which have stress drop estimates from both methods. We find that SR corner frequencies are systematically higher than SDC corner frequencies, consistent with the study by Shearer et al. (2019). We obtain a proportionality factor

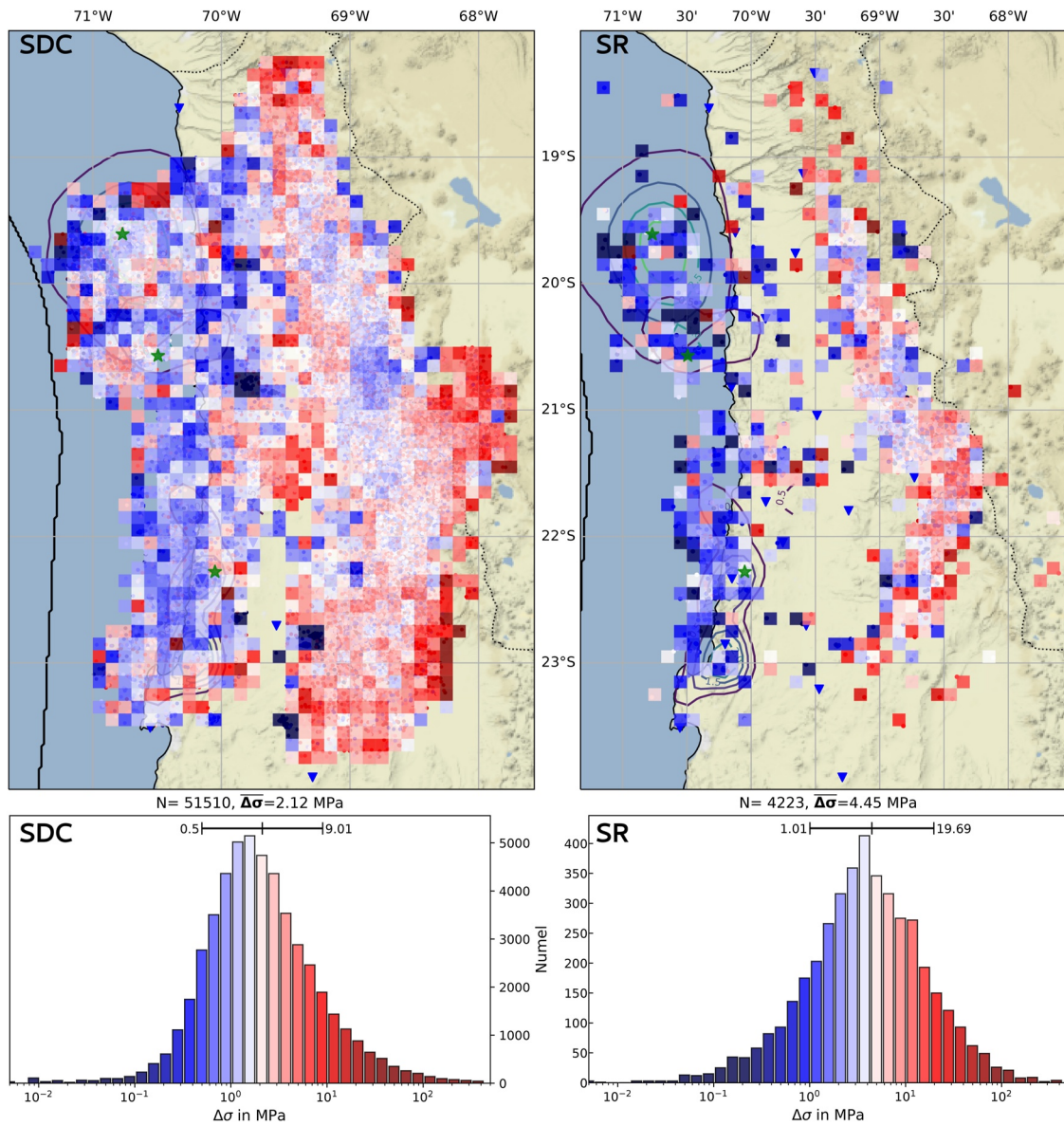


**Figure 6.** Stress drop distributions in the target region computed by the spectral decomposition approach (SDC) and by the spectral ratio approach (SR). Each  $0.1^\circ \times 0.1^\circ$  grid cell represents the median value of all calculated stress drop estimates within the cell. No smoothing is applied. The colors correspond to the histograms on the bottom, which show log-normal distributions in both cases. Stress drop estimates for 51,510 events are obtained with a median of 2.12 MPa for the SDC approach and 4,223 resulting stress drops with a median of 4.45 MPa for the SR method. The standard deviations are indicated above the distributions. Note the good consistency between results of both methods.

of 0.75 between the two corner frequency families ( $f_{c_{SDC}} = 0.75 \times f_{c_{SR}}$ ). With this, stress drops translate as  $\Delta\sigma_{SDC} = 0.42 \times \Delta\sigma_{SR}$ . Shearer et al. (2019) carefully compared the two approaches and found systematic differences of the calculated stress drops. In order to reconcile the absolute values of both methods, they proposed to fix the corner frequency of the EGF event ( $f_{c2}$  in Equation 6) in the SR method to an optimized value which is then used for all ratios in the data set. We do not focus on the issue of adjusting the methods as we have demonstrated the principal similarity and especially since almost all SR results have an equivalent stress drop estimate from the SDC method.

Summarizing this paragraph, we have shown the high level of similarity of results obtained by both methods. They are qualitatively similar, but the number of SDC estimates is significantly higher. Also they include stress drop estimates for basically all events with SR solutions. The validation of similarity was necessary, as we can

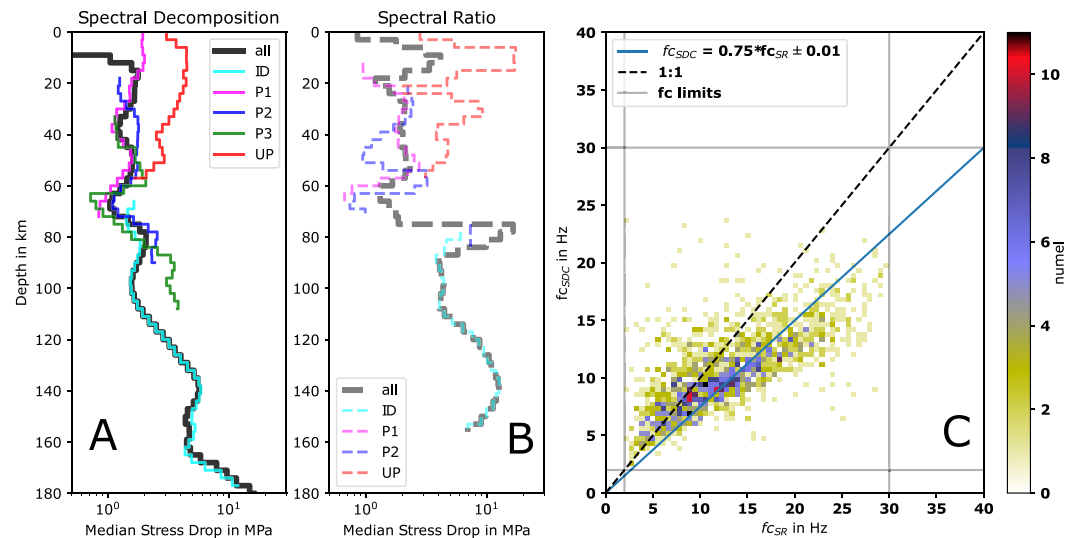


**Figure 7.** Median stress drop variation with depth for the SDC (a) and SR (b) results, smoothed over three bins (9 km), color coded after event classification. SR results scatter significantly more due to the limited event count and sparser coverage. Note the principally good consistency of the curve shapes between results of both methods, for both the overall depth variation and the class wise variations. (c) Density plot of corner frequency estimates for 1,700 events ( $M \geq 2.6$ ), for which stress drop values were found by both methods, the spectral ratio and the spectral decomposition approach. Color indicates event count per cell. The gray lines mark the corner frequency resolution limits. Density is high in the center of the cloud, especially along the regression line, expressing a general agreement between both methods. The obtained relation between results is  $f_{c_{SDC}} = 0.75 \times f_{c_{SR}}$  which translates into  $\Delta\sigma_{SDC} = 0.42 \times \Delta\sigma_{SR}$ .

now focus only on the SDC results in greater detail, in the following. For the interested reader, we include SR result based figures for each of the following SDC results based figures in the supplement.

#### 4.2. Stress Drop Estimation Results

The spectral decomposition method yields stress drop values for 51,510 events. For each event, the value is calculated as the median of all available stress drop estimates originating from multiple cells (i.e., different gEGFs) and from both P and S phases. The resulting stress drop distribution is shown in Figure 6, where the event-wise stress drops are averaged on a regular grid using  $0.1^\circ \times 0.1^\circ$  cells and color-coded according to the color scheme provided in the corresponding histogram. The stress drop histogram shows a well-defined log-normal distribution with a median value of 2.12 MPa. There is an apparent systematic difference between the stress drops in the western and the eastern part of the study region.

An exemplary west-east side view of the entire depth range from trench to about 180 km depth (Figure 8) better resolves the seismically active domains responsible for the stress drop variation which is evident in the map view. It clearly demonstrates the distinct and systematic differences of stress drop associated with specific regions. The seismicity along the plate interface clearly sticks out with low stress drop values whereas the upper plate crustal events have on average relatively high stress drops. The two interface-parallel bands of seismicity show a mixture of low to medium values, and the intermediate depth seismicity band exhibits a depth-dependent increase of stress drop. Hence, the apparent segmentation of the subduction zone based on deviations in stress drop value corresponds well to the event classification from Sippl et al. (2023). Consequently, we analyze the stress drop variability based on the predefined event classes in the following.

Figure 9 illustrates the class-wise histograms for stress drops, magnitudes, corner frequencies and S- wave velocities. All classes except the mining events (MI) show log-normal distributions of stress drop. 97.5% of the estimates lie between 0.1 and 100 MPa. Their median values are 1.4 MPa for class P1 events, 1.7 MPa for P2, 2.1 MPa for P3, 3.3 MPa for UP and 2.3 MPa for class ID events. For each class, the spatial distribution of stress drop in map view is plotted separately in Figure 10.

The spatial availability of stress drop estimates generally follows the variation of seismic activity. In consequence, the results for each event class are limited to cells of sufficient earthquake occurrences. Numbers of upper plate

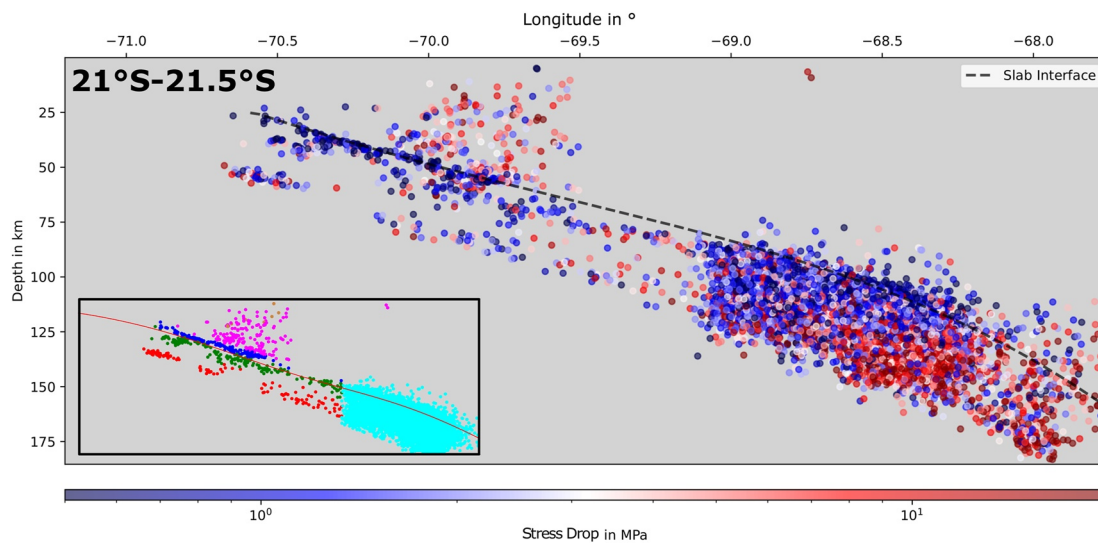


**Figure 8.** West-east stress drop slice at 21.0°S to 21.5°S. Color indicates single event SDC stress drop value. The inset shows the same section with coloring corresponding to event class, similar to Figure 1. Note the clear visual separation of UP and P1 class events. The low stress drop values along the interface are traceable even into the deeper ID cloud. Also, an increasing stress drop with depth in the ID cloud is clearly visible. The slab interface estimate displayed stems from Sippl et al. (2018).

events, for example, are higher in the latitude range of the Iquique event (approx. 20°S), which had a shallow rupture origin and activated a shallower part of the megathrust and many crustal events. In contrast, the smaller Tocopilla event in the south, which had a comparatively deep origin and rupture surface did not have large impact on crustal seismicity. Consequently, fewer UP event stress drops could be computed in the southern region, leading to non-uniform sampled average values of the stress drop distributions. Such sparsity is most apparent in the UP and P3 classes. The interface, in contrast, was activated by both megathrust events (cf. Figure 10), leading to large amounts of seismicity in the corresponding areas and their surroundings, which enables a good coverage with stress drop estimates in the P1 class. This heterogeneity of existing data points has to be considered when interpreting the overall results.

Next to the SDC results Figure 6 includes the results from the spectral ratio approach. Limited by the number and availability of suitable EGFs, 62,115 stress drop estimates are found for 4,223 events. Again, each final estimate is the median of the stress drop estimates for each target event, which originate from different possible EGFs as well as the use of both P and S phases. The overall spatial distribution of results is similar to the distribution from the spectral decomposition method, and also the stress drop variation appears to be similar, except that a smaller area is covered (fewer estimates) and that the overall median is higher (4.45 MPa). Despite this discrepancy, the median values between estimates of different event classes keep about the same relative differences with P1, P2, P3, UP, and ID having average stress drop values of 2.0, 1.9, 1.9, 4.0, and 5.2 MPa, respectively. Note that especially P2 and P3 include results for only few events. An equivalent to Figures 9 and 10 for spectral ratio results can be found in Supporting Information S1 (Figures S12 and S13).

Different profiles (west-east, north-south, depth, distance to interface) for the entire stress drop ensemble along with the median short range stress drop variation are shown in the supplement Figure S13 in Supporting Information S1 as well as for each class separately in Figures S14–S20 in Supporting Information S1, for results of both methods.

### 4.3. Detailed Observations

In this section we describe the main stress drop pattern separately for each event class. The observations mostly relate to the depth-dependent variability (Figure 7), the histograms (Figure 9) or the class-wise maps (Figure 10). More details, such as the variation of the short range median stress drop (for easting, northing, depth, and distance to interface) for each separate class is displayed in Figures S14–S20 in Supporting Information S1.

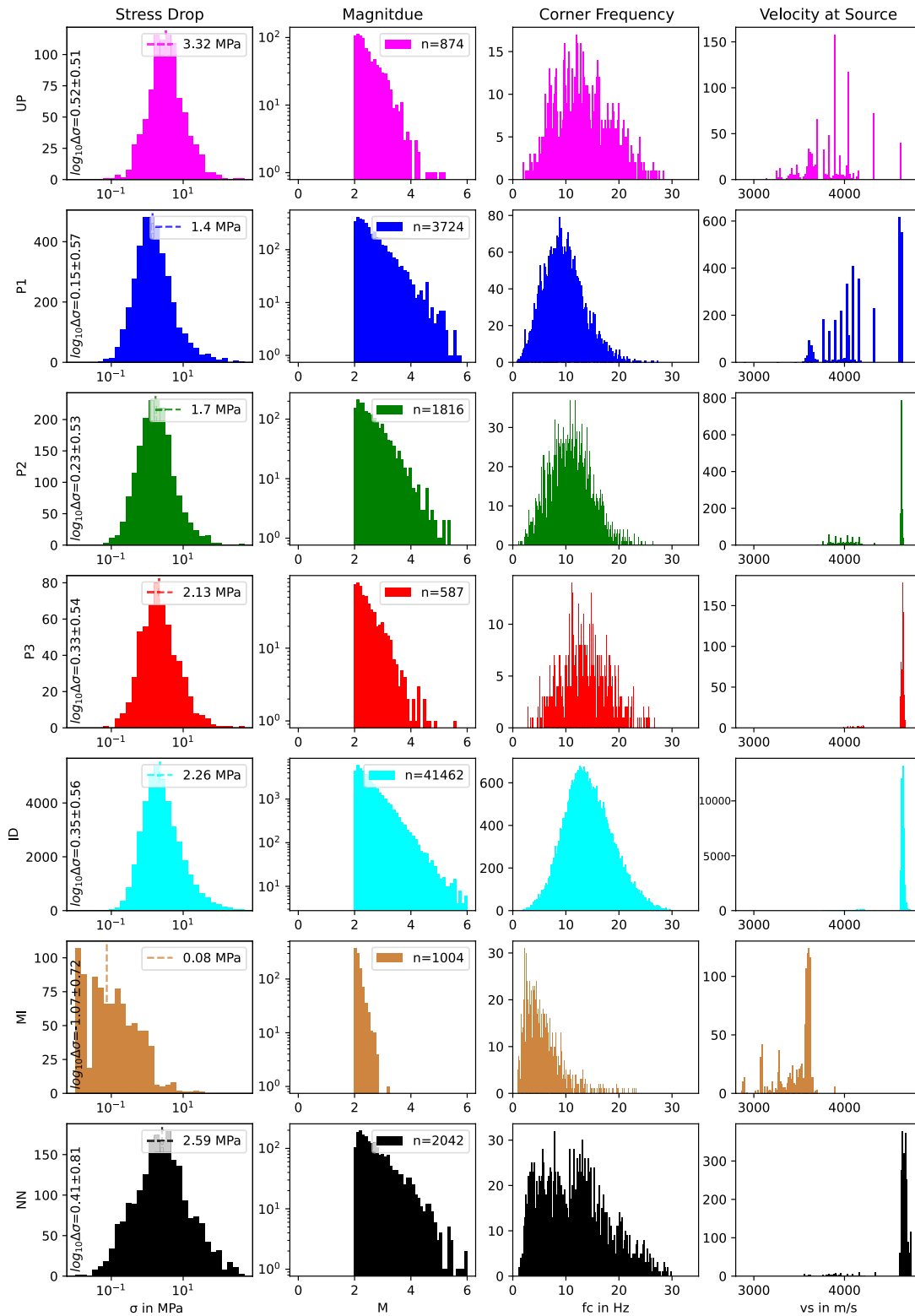


**Figure 9.** Distributions of SDC stress drop, magnitude, corner frequency and S velocity at the source for UP, P1, P2, P3, ID, MI, and NN classes, from top to bottom. Stress drops were calculated based on the displayed corner frequencies, seismic moments (from the displayed magnitude distribution) and the S wave velocities at the source (Equation 3). Median stress drops are displayed in the stress drops column legends and total event number in the magnitude column legends. Note the difference in median stress drop between classes, for example, the plate interface (P1) showing the lowest median value and intermediate depth events (ID) or upper plate events (UP) significantly higher median values.

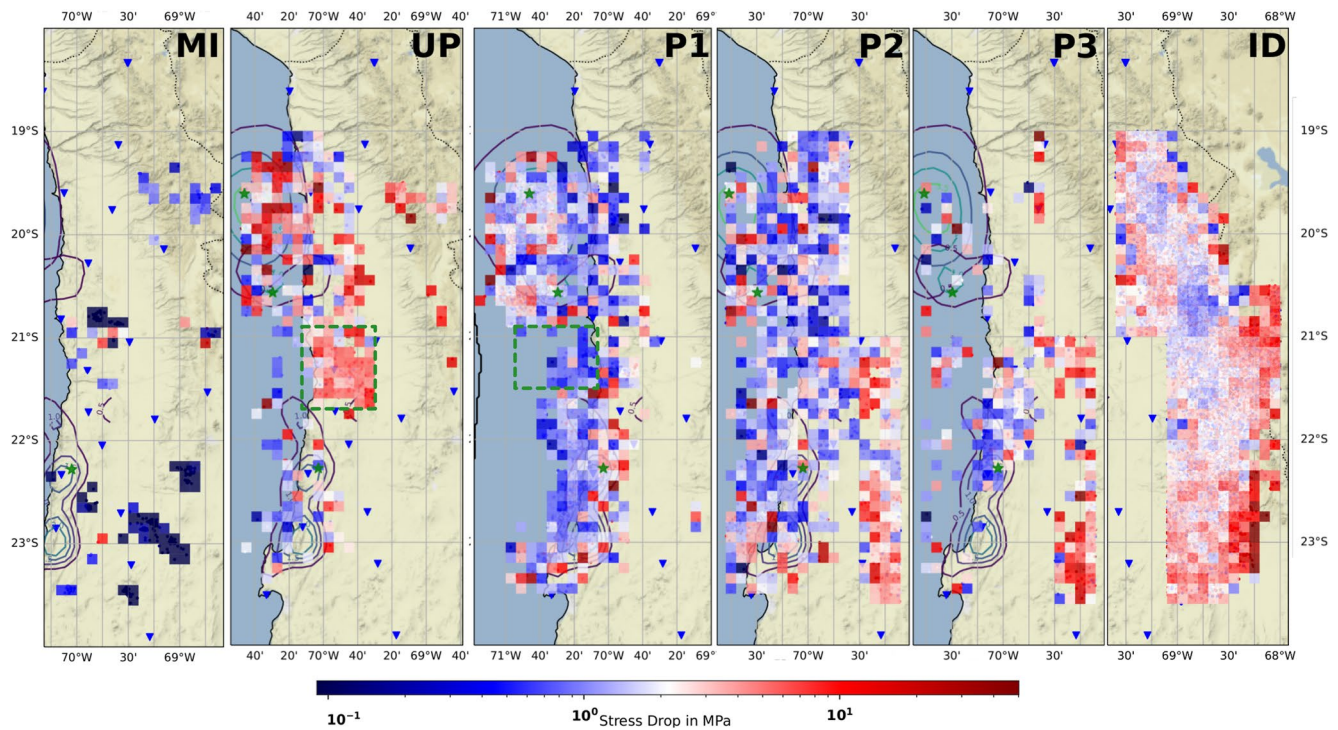


**Figure 10.** Stress drop distributions in the target region computed from spectral decomposition approach separated into the classes MI, UP, P1, P2, P3, and ID from left to right, respectively. The color scheme is the same as in Figure 6. Histograms and median values for each class of events are displayed in Figure 9. A detailed description on the spatio-temporal variability of stress drop are found in the text. Two regions of special interest are highlighted by green dashed boxes in the UP and P1 maps, showing particularly high and relatively low stress drops, respectively. The map for the NN class is shown in Figure S14 in Supporting Information S1.

### 4.3.1. Spatial Variation

**UP** Upper plate seismicity shows a comparatively high median stress drop of 3.32 MPa. We observe an increase of stress drop with depth from 2 MPa to about 4.5 MPa in the uppermost 20 km, below which the median stress drop decreases slowly with depth back to about 2 MPa (cf. Figure 7). Most upper plate stress drop estimates are from the Iquique mainshock area between 19.2–20.6°S, and from the seismically highly active region just south of it (cf. Figure 10). The highest median values are found from 20.0 to 20.2°S (3 MPa) and 21.0 to 21.6°S (4 MPa). The upper plate events show a steady increase of stress drop with distance to the interface for the first 30 km upward (Figure S14 in Supporting Information S1). There are two major continuous patches of increased upper plate stress drops observed (Figure 10). One is located above the main rupture patch of the Iquique event, a region that was struck by the crustal Mw6.7 Iquique foreshock and its aftershocks (Schurr et al., 2014, 2020). The other one is located at 21.0°S–21.7°S, starting from the coast and extending about 70 km toward east (green dashed box). Seismicity rates in this area are reportedly elevated, and Sippl et al. (2018) proposed a correlation to the decreased locking observed by geodetic studies.

**P1** Interface seismicity, labeled as P1, poses the second-largest class of events ( $n = 3,724$ ). It includes events from near the trench to about 69.6°W inland and almost completely covers the area between 19°S and 23.5°S. It shows the lowest median stress drop of all classes (1.4 MPa) of natural seismicity. The values found closest to the plate interface are even slightly lower, and increase with distance (cf. Figure S15 in Supporting Information S1) both in down and upward direction. The short range median remains stable at 2 MPa down to 15 km depth, and then decreases down to 1 MPa at 40 km. Below at 50 km, a local maximum of 1.8 MPa occurs, followed by values below 1 MPa at around 65 km depth (cf. Figure 7 and Figure S15 in Supporting Information S1). The stress drop distribution on the plate interface is dominated by fore- and aftershock sequences of the Iquique earthquake and the Tocopilla earthquake. The stress drop distribution in the Iquique region shows low to average values close to the hypocenter locations of both main shock and aftershock (Figure 10). At the western and northern rim of the main shock, high stress drop values are observed. Just between the main and aftershock slip surfaces, a band of low stress drop values is located, similar in values to those located at the southern end of the aftershock slip area.

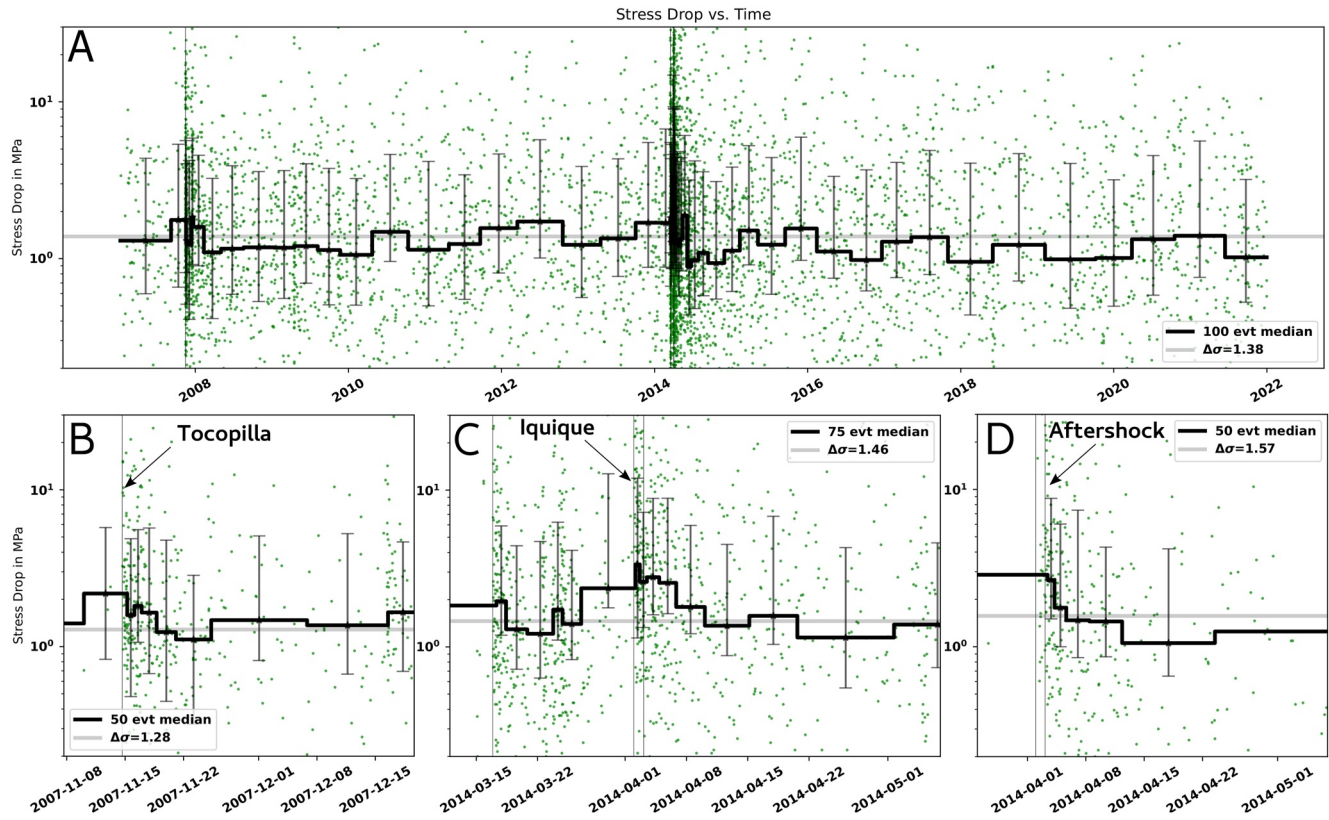


**Figure 11.** (a) Stress drop distribution versus time for events limited to longitudes west of  $70^{\circ}\text{W}$  for the entire observation period. The median is computed over 100 events per bin. Error bars represent the 25% and 75% percentiles. No smoothing is applied. Gray vertical lines denote the Tocopilla and the Iquique event. (b) Five weeks of stress drops from the  $M_w 7.7$  Tocopilla aftershock area ( $\text{lat} \leq -70, -21.5^{\circ} > \text{lon} > -23.25^{\circ}$ ). The vertical line is the Tocopilla origin time. (c) Stress drops from the Iquique aftershock area ( $\text{lat} \leq -70, -19^{\circ} > \text{lon} > -20.25^{\circ}$ ) 3 weeks before to 5 weeks after the Iquique event. Ray vertical lines denote the  $M_w 6.7$  foreshock, the  $M_w 8.1$  Iquique event, and the  $M_w 7.6$  aftershock, respectively. (d) Stress drops from the  $M_w 7.6$  Iquique aftershock area ( $\text{lat} \leq -70, -20.25^{\circ} > \text{lon} > -20.75^{\circ}$ ). The second vertical line is its origin time. The gray horizontal line is the long term stress drop median for the corresponding region. For all large events, the stress drop values are elevated close to the origin times of the main shock, followed by a rapid but not instant decline to values below the median, followed by a return to average values within a few days to weeks.

The high slip regions of the Tocopilla event are characterized by low to average median stress drop values, while the down dip edge is dominated by high values and the up dip edge is surrounded by low values. The region north of the Tocopilla event rupture area shows a large patch of low stress drop values (green dashed box), covering parts of the gap northwards to the Iquique event aftershock area. Note that this low stress drop patch directly borders the large high stress drop region to its east observed in the upper plate, as described above. Also note that, although the P1 class is only defined down to a depth of about 65 km, low stress drop values along the interface are observed down to a depth of at least 125 km (see Figure 8).

**P2** The first seismically active band below the interface has a slightly higher median stress drop (1.7 MPa,  $n = 1,816$ ) than the interface seismicity. Similar to P1 it covers a large region almost completely. Maybe due to its lower event count the map shows more fluctuations and less well defined low/high valued patches. Still, the stress drops close to the hypocenters of the Iquique event and its main aftershock are recognizable higher than in P1. The low stress drop band between the two major events is also indicated, similar to the low stress drops in the seismic gap between the Iquique aftershock and the Tocopilla earthquake, which here extends slightly more to the east. In the central-eastern and southeastern part, some patches of elevated stress drops are observed. The median stress drop depth variation is similar to the P1 curve, having a peak of 2 MPa at about 50 km depth, followed by a decrease. From 65 km on, an increase to about 3 MPa occurs (Figure 7).

**P3** The same variation with depth is seen for the P3 class events, which are part of the second interface parallel band. The limited amount of events ( $n = 587$ ) is spatially separated into several areas, like the northern part of the Tocopilla earthquake slip surface, associated with low stress drop values and some deeper and more eastern cells,

where median values reach up to 6 MPa. Interestingly, this is a higher value than for the neighboring cells, located in the intermediate depth class (ID). Especially the latter group of comparatively deep events is responsible for the relatively high median value (2.13 MPa) found for this class.

**ID** The ID class (or else called IDEs) is the largest group ( $n = 41,462$ ) and shows a higher median of 2.26 MPa compared to the Px group. It is the only class where the stress drop map is locally fully continuous and many cells exceed 1,000 event members. While the ID event stress drop map is dominated by medium to high values (Figure 10) there exist two patches of lower than average stress drop at about  $19.5^{\circ}\text{S}$  and at  $20.75^{\circ}\text{S}$ . Especially the latter region is seismically the most active region in the entire data set (Sippl et al., 2018) and thus, it contributes many low stress drop values to this event class which otherwise would have an even higher median value. In its shallowest part the depth variation is similar to that of the Px group, with a minimum (1.5 MPa) at about 75 km depth, followed by an increase to 2.2 MPa at about 90 km depth and, after some short decrease, a more rapid rise to about 8.5 MPa at a depth of 140 km. Further down the increase of stress drop appears to cease at 175 km below which stress drops increase again up to values exceeding 10 MPa. Note that this class of events shows the highest range of median stress drop variation with depth. Several possible reasons for the increase will be discussed later.

**MI** We obtain stress drop estimates for 1,004 events from the mining class with a very low median stress drop of 0.08 MPa. 876 of them were labeled MI in the IPOC catalog and 128, which initially were classified as UP events, were reassigned to the MI class because of their particularly low stress drops and their clustered and shallow locations. It is interesting to note that only a small fraction of the events exceed stress drops of 1 MPa while many estimates significantly undercut 0.1 MPa. The statistical distribution of the mining-related events stands out against the other classes of tectonic events and deviates strongly from a log-normal shape as seen in Figure 9.

**NN** The locally less well constrained events from the NN class are basically split into two major groups. The first group are those events which lie far offshore and have poorly constrained depths. The second group are events located far east of the network mostly at great depth ( $>150$  km). Here, the location accuracy is also decreased. Hence, the stress drop values suffer from possibly wrongly assigned S wave velocities. For example, for the shallow group, almost exclusively lower plate mantle velocities are used. Should any of them lie at or closely below the interface, their stress drops would be much higher when using lower plate crustal velocity. The stress drop distribution from Figure 9 reflects the separation of stress drops into two groups by a comparatively large standard deviation and a bimodal shape of the corner frequency distribution. Including this class here has two main reasons. One is the additional depth extent (160–180 km) covered almost exclusively by this event group, and the second is the consistency of the processing with the complete IPOC catalog.

Similarly, as the MI events, we do not further discuss their properties or interpret their stress drops. The corresponding stress drop map for this class is shown in the supplement Figure S14 in Supporting Information S1.

#### 4.3.2. Temporal Variation

Stress drops do not only vary in space, but also in time (e.g., Allmann & Shearer, 2007). We observe such variation for shallow, predominantly interface and upper plate seismicity in Figure 11. Strikingly, the one hundred event median shows maxima at the occurrence times of the large interface events. We therefore show narrower time frames for spatially limited areas around four major earthquakes: the  $M_w 8.1$  Iquique event, its  $M_w 6.7$  foreshock, its  $M_w 7.6$  aftershock and the  $M_w 7.7$  Tocopilla event. All stress drop curves have similar shapes. Initially, at occurrence time, the median stress drop is high, up to multiple times the long term median of the specific region. In the following days, a decline of stress drop values down to values slightly below average is observed, followed by a recovery back to average values. The decay time is longest for the largest of the four and shortest for the smallest main shock.

This behavior has already been described in Folesky et al. (2021) for the Iquique event. There, the variability was attributed to the increased moment rates during the immediate post-seismic interval. We observe the same effect here for three additional large magnitude events. To illustrate the influence of the temporal moment rate variability, we plot the time-dependent stress drop variation scaled by event moment rate in the supplement (Figure S25 in Supporting Information S1). Please note, that one potential key aspect in this observation is the apparent moment dependent scaling in our results, discussed later in the text. Also, in the high event rate aftershock period, event detection might be incomplete in the IPOC catalog, favoring large magnitude events which would additionally bias the above observation.

The stress drop scatter in each time bin is significant, as indicated by the 25% and 75% percentiles. The percentiles log-distance is stable between time steps and corresponds well to the overall stress drop standard deviation



(Figure 7). This can be understood as a consequence of the natural log-normal distribution of the stress drop. The median stress drop variation between steps is significantly less than the average percentile distance. As percentile markers in Figure 11 always follow the median stress drop variation from step to step, we stick to the description of variability via the median stress drop.

## 5. Discussion

In this section, we first discuss the results of this study in the context of other stress drop studies. Next, we consider implications of the used methods, limitations and possible biases. We then highlight the most interesting aspects of our stress drop distribution and show possible correlations with other research in the northern Chilean subduction zone. In doing so, we exhibit the potential of a comprehensive stress drop map to contribute to interpretations of the tectonic state of, for example, the megathrust, or to questions of source physics and stress distribution in a subduction environment.

### 5.1. Overall Results

The principal range of obtained stress drops in this work is between 0.1 and 100 MPa (for 97.5% of estimates), a well accepted corridor for natural seismicity found in multiple studies for many events and a broad magnitude range (e.g., Allmann & Shearer, 2007, 2009; Tian et al., 2022; Uchide et al., 2014). Median values vary significantly less, ranging from 1 MPa for shallow events to 15 MPa for the deepest in this data set, as well as from 1.4 to 3.1 MPa between different event classes. Median values for spectral ratios are on average about twice as high. This shows that although median stress drop is found to differ between different regions, depths, and classes with good consistency between methods, a single event cannot unambiguously be assigned to a class based solely on its stress drop value. This is also a consequence of the natural log-normal distribution of the stress drop (Figure 9).

Especially absolute values have to be handled with care. Not only the parameters in the chosen source model, but also the methods for determining the corner frequency may introduce additional differences. It is clear that different source model choices, that is,  $k$ -values, also produce large deviations in absolute stress drop (e.g., Ji et al., 2022; Kaneko & Shearer, 2015). Hence, it is beneficial to process many events similarly and interpret results based on relative differences, if possible confirmed by multiple methods (e.g., Pennington et al., 2021).

For northern Chile, only limited stress drop data has been reported, so far. For example, Cabrera et al. (2021) compute stress drops for six large magnitude events located at shallow intermediate depths in northern Chile. They use kinematic source inversion and find absolute stress drops of 7–30 MPa. These values seem relatively low compared to our results of large magnitude intermediate depth seismicity.

Derode and Campos (2019) estimated corner frequencies from attenuation-corrected spectra for 96 events in northern Chile. They do not provide values for the stress drop, but note that the corner frequencies of intermediate depth earthquakes are significantly elevated compared to shallow depth earthquakes, which would lead to elevated values for the stress drop, consistent with our results. They emphasize that the stress drop depends strongly on the unknown rupture velocity, which can vary from event to event, which is also true for our study. Folesky et al. (2018) calculated rupture velocities for small to moderate earthquakes in the Iquique region. The resulting average velocity fits well with the assumed value of  $0.7\beta$  from this study, but the reported scatter of velocity values is quite large, although the study was limited to shallow seismicity. Therefore, we note that variable rupture velocities are an important source of perturbation to consider. For example, the increase in observed stress drop could be explained simply by a change in the assumed average  $v_r/v_s$  with depth. We did not observe a change in the  $f_c/f_c^s$  ratios with depth, which would have been a clear indication of a change in rupture velocity (Kaneko & Shearer, 2014, 2015).

### 5.2. Method and Limitations

In this study, similar to Folesky et al. (2021), we observe a clear dependence of stress drop on moment (Figure 12a), which contradicts the invariance hypothesis of stress drop scaling for our data set in northern Chile. We fit a linear relation ( $\log_{10}(\Delta\sigma) = \varepsilon_0 + \varepsilon_1 \log_{10}(M_0)$ ) to stress drop estimates over separate magnitude bins (e.g., Trugman & Shearer, 2017) and we obtain  $0.4 < \varepsilon_1 < 1.09$ . This indicates a moderate to strong dependence of stress drop on moment. Note, that the elevated  $\varepsilon_1$  values for the M2-2.5 and >M4.5 bins are an indication for

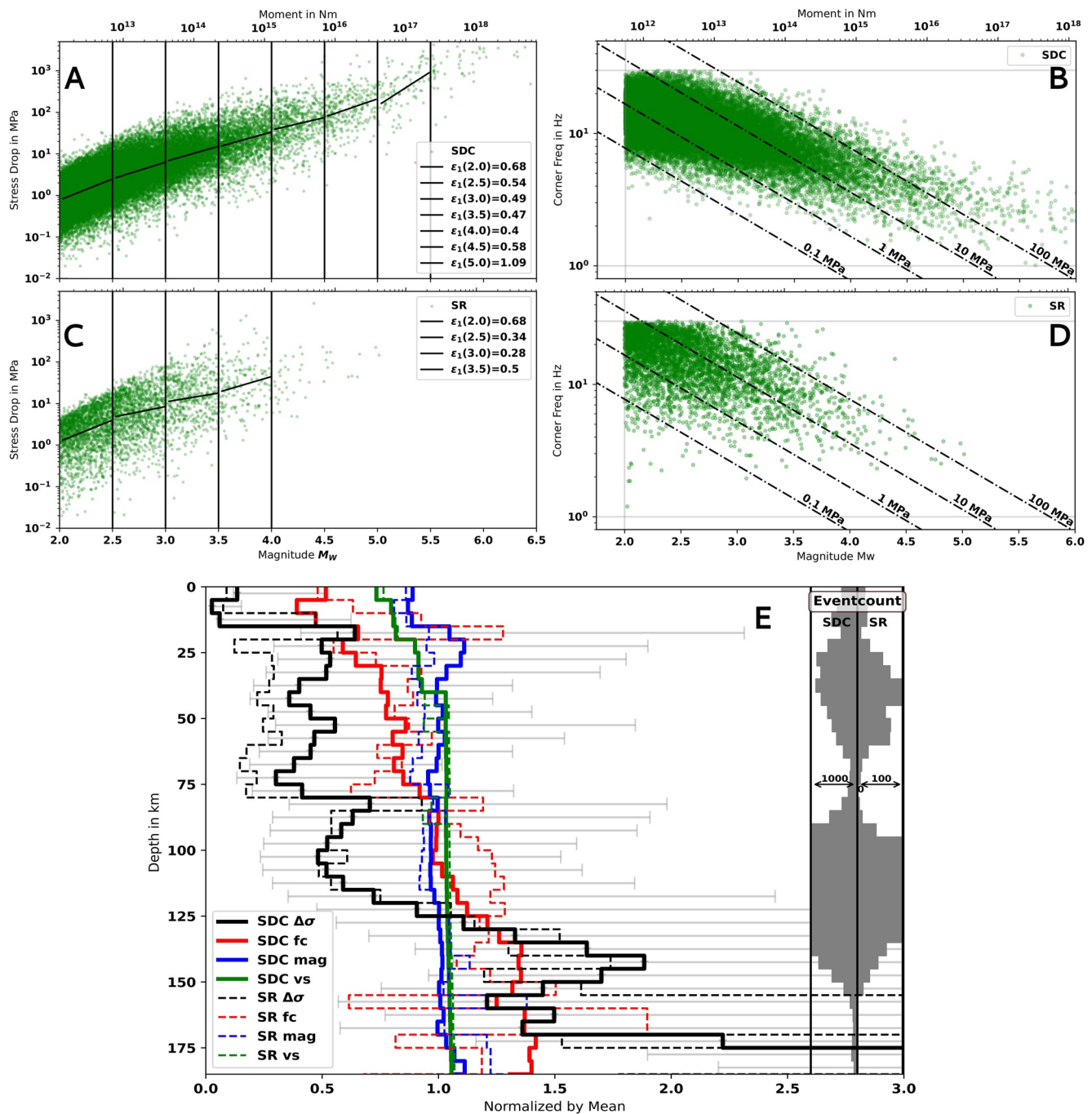


**Figure 12.** (a) SDC stress drop (no MI events) against moment. The black line is the bin wise linear fit of the SDC data, (b) shows corner frequency versus moment. Gray lines indicate the frequency limits. Panels (c) and (d) are similar to (a) and (b) but for SR results. (e) Depth against normalized stress drop, normalized corner frequency, normalized magnitude, and normalized S wave velocity, demonstrating that the main driver of increased stress drop with depth (>80 km) is the increase of corner frequency. Solid lines are SDC medians, dashed lines are SR medians. Gray error bars show SDC stress drop percentiles. On the right the event count per bin is shown capped at 1000 (SDC) and 100 (SR) events per bin.

a possible bandwidth limitation/event selection bias (Ide & Beroza, 2001) at the magnitude interval limits. As a consequence of the high frequency spectral limit (30 Hz), small magnitude stress drop estimates might have too small  $f_c$  estimates or get deselected, entirely. This could skew the distribution in that bin. The top bins could be affected in the same way. The inner bins, however, also show a clear moment dependence, which cannot be explained similarly. As reported in Folesky et al. (2021) more restrictive quality criteria for spectra included in the analysis may moderately decrease the  $\epsilon_1$  parameter, but the clear positive dependence remains.

Trugman and Shearer (2017), have explicitly shown, that there is a fundamental trade-off between  $n$  and  $\epsilon_1$  (the scaling factor) when using the spectral decomposition algorithm (SDC). According to them, to obtain scale invariance, the spectral falloff, most commonly set to  $n = 2$ , must be allowed to vary to lower values. They explain this by an apparently higher spectral content at high frequencies in larger events than predicted by a standard Brune type spectral model. For example, Allmann and Shearer (2009), have used  $n = 1.6$  for analyzing events with magnitude larger M5.5 to obtain scale invariance.

Alternatively, one can drop the scale invariance hypothesis and allow for variable stress drop in the spectral stacking procedure, that is, a more data driven ansatz while keeping  $n$  fixed to 2. According to Trugman and Shearer (2017), both variants are indistinguishable in terms of rms-misfit. In our work, the second approach was taken, by applying the SDC technique called SNSS, initially described in Chen and Abercrombie (2020). As a consequence, stress drop scales with moment as described above. Using similar assumptions, for example, Prieto et al. (2013), Trugman and Shearer (2017), or Pennington et al. (2021), report scale dependency comparable to our results ( $\Delta\sigma \sim M_0^{0.2-0.8}$ ), as opposed to other studies which report a general scale invariance of stress drop (e.g., Abercrombie (1995), or Shearer et al. (2006)). Please note that moment dependent stress drop is also observed in the SR results of our study, where we find  $\Delta\sigma \sim M_0^{0.3-0.7}$  (Figure 12c). Moment dependent stress drop was reported in other SR studies as well, for example, Calderoni et al. (2013). On the downside of allowing the data driven concept, the strong scaling leads to unreasonable high stress drops for large magnitude events in our data (Figure 12a).

Other sources of bias are potential event selection and bandwidth limitations. To systematically check whether the initial quality criteria (e.g., SNR) introduce a significant event selection bias (Ide & Beroza, 2001) and how the bandwidth limitation can affect the results, we compared the IPOC catalog magnitude frequency distribution with that of the stress drop result catalog. We find that only a small and stable fraction of events in each magnitude bin did not allow computing stress drops (<10%, Figure S27 in Supporting Information S1) indicating no severe apparent selection bias. The effect of bandwidth limitation is much harder to assess. The overall distribution of computed corner frequencies (Figure S28 in Supporting Information S1) shows the limited amount of events ( $n = 163$ ) which got discarded due to too high  $f_c$ . They practically have no impact on the overall statistic. A check on the 5% variance bounds for the estimated corner frequencies (Viegas et al., 2010) does not reveal systematic frequency underestimation at the high limits (Figure S29 in Supporting Information S1).

From other studies, however, one might expect more high corner frequency events where  $f_c > 30$  Hz (even if they are later discarded during processing). The apparent lack of such events in our data could be an effect of the relatively sparse station coverage in northern Chile. Average event station distances, especially for the ID events, which pose the great majority of datapoints, are easily in the 100 km range. If attenuation removed the high frequency content, we would not be able to recontract it, even with highly suitable Green's functions. This might also effect several events below  $f_c = 30$  Hz.

In sum, we have applied a well accepted processing technique to estimate earthquake stress drop which is data driven, and we assumed the spectral falloff rate of  $n = 2$ , most commonly used in spectral studies. In doing so, we obtain a dependence of stress drop on seismic moment which is persistent at all magnitude bins and which is observed in our SR results, too. For large magnitudes this leads to unphysically large stress drop estimates and hence can be considered inappropriate. For small magnitude events, band limitations might lead to missing high stress drop events, increasing the apparent moment dependency. Nevertheless, we prefer the data driven approach over the forced scale invariance choice.

To underline the robustness of both the overall results as well as the localized observed variability of our results, we add a stress drop map similar to Figure 6 to the supplement (Figure S26 in Supporting Information S1) where we have limited results to events of magnitudes between M2.8–M4.5. It features a very similar distribution of stress drop through the subduction zone.

### 5.3. Depth Dependence and Local Variability

A depth dependence of stress drop was reported in many studies (e.g., Boyd et al., 2017; Trugman, 2020; Uchide et al., 2014), while others find no such evidence (e.g., Shearer et al., 2006). A conclusive explanation of depth dependent stress drop or a convincing correlation to other parameters is still missing. Whether stress drop increases in the crust was recently discussed in detail by Abercrombie et al. (2021), who find that most studies probably

overestimate the depth dependency by different ways of under-correcting the depth dependent attenuation. They state that using a spectral ratio approach with good EGFs should principally be unaffected by such problems. We do not find significant qualitative differences of results of our two approaches concerning this question. And we observe both, a stress drop increase in the crust for  $z \leq 20$  km from 2 to 4 MPa and below, a median stress drop that decreases slowly back to about 2 MPa over a range of 40 km (Figure 7 and Figure S15 in Supporting Information S1) with minor fluctuation. In northern Chile, continental crustal thickness ranges up to 60 km (Patzwahl et al., 1999) which is also represented in the utilized velocity model (Figure S30 in Supporting Information S1). Note that the UP class also contains seismicity from the subduction wedge and that the Moho deepens from west to east with the plate interface deepening. Additionally, stress drop sampling in the upper crust is not uniform but concentrated to several regions. The behavior of the average stress drop median with depth might therefore not be unbiased by the subduction geometry and most likely it is not indicative for intra-plate stress drop variability.

The median value of stress drop combined for all classes shows three relative maxima at 20 km, 55 and 85 km depth (Figures 7 and 12e). At these depths median stress drop varies only between 1.25 and 2.5 MPa. Note, that sampling (number of stress drop estimates per depth bin) is not uniform (Figure 12e). At greater depths, (>100 km) a consistent increase to values up to 8.5 MPa is observed, followed by a plateau and another subsequent increase to values above 10 MPa. To investigate the driving parameter for the increase, we plot corner frequency, magnitude and S wave velocity against depth (Figure 12e). The top 60 km show a complicated behavior of the three curves, but it appears that medium magnitude values remain stable below 40 km and mean velocity is basically constant below 60 km depth. Solely the median corner frequency estimate increases almost steadily with depth, causing the rise in stress drop. Therefore, we conclude that the increase of stress drop with depth is mostly driven by an increase of corner frequency. This holds for both the spectral decomposition and the spectral ratio method (with significantly stronger fluctuation), and we consider this result robust. Note, that different depth might be sampled very differently, as shown in Figure 12e.

Interestingly, and different from this observation, the variability of stress drop with time found for the major earthquakes in the catalog region (Figure 11) appears to be primarily driven by increased moment release rate, rather than temporally elevated average corner frequency (cf. Figure S25 in Supporting Information S1). Indeed, during that period, average corner frequencies appear reduced, which is expected if predominately larger events occur. This reduction, however, does not suffice to compensate the increased moment which results in increased stress drop. Once this effect decays, the overall median stress drop returns to its initial value. Also, on a longer timescale, its alteration is not permanent. For example, the difference of median stress drop for events that occurred earlier than 4 weeks before the Iquique event and events that occurred later than 4 weeks after the Iquique event is about 0.03 MPa. For the Tocopilla event, this difference is 0.09 MPa. A similar observation was made in California, where the 2004 M6 Parkfield earthquake reportedly did not permanently change the stress drop pattern (Allmann & Shearer, 2007).

To our knowledge, a consistent, continuous and comprehensive analysis of the stress drop pattern over the broad depth range of 0–180 km as performed in the present study has not yet been reported elsewhere. We can therefore only compare with studies that cover subdomains of this range. Allmann and Shearer (2009) studied the distribution of stress drop for global seismicity and found evidence of a downward increase in stress drop from a depth of 30 km. Şen et al. (2015) analyzed the rupture duration of aftershocks from the 2010 Mw8.8 Maule earthquake, Chile, at 35°S and noticed variability in normalized rupture duration with a minimum at 40 km depth. Since the source duration is inverse to the corner frequency, a reduction corresponds to an increase of stress drop. However, in both studies, no results are calculated below 60 km depth. In Japan, Uchide et al. (2014) studied the variation of stress drop in the broader region of the 2011 Tohoku earthquake. Their analysis includes events to a maximum depth of 80 km. They find a sharp increase in stress drop between 30 and 60 km accompanied by plateaus with constant median stress drop below and above. They have no conclusive interpretation for the increase or the plateaus they observed.

Other studies focus on deeper events, such as Poli and Prieto (2016), who estimate the stress drop for global ID events and deep events based on estimates of the duration of the source time function. They find mean stress drop values of about 10–20 MPa for their shallowest events at about 150 km depth, with no subsequent increase. Given the general variability in stress drop estimates among authors and methods, these absolute values fit well with the estimates that we obtained for the deepest events in Northern Chile, which also indicate a cessation of stress drop increase near the depth limits of our study. Tian et al. (2022) analyze stress drops from intermediate depth to

deep events in the Tonga region and find average values around 5.6 MPa at 90 km depth, followed by decreasing median values to a minimum of 3 MPa at 170–250 km and then by an increase back to 6 MPa at greater depth. They report that they can best associate zones of high stress drop with areas of high plate deformation. In northern Chile, the plate undergoes strong geometric changes as it bends at shallow depths (<60 km), stops bending below (60–100 km), followed by bending that ends with a strong downward kink (Sippl et al., 2019, 2023). The strongest geometric deformation is observed between 100 and 140 km depth (Sippl et al., 2022), where the plate is bent to a significantly steeper subduction angle. As the depth of this bending process varies laterally, an increasing number of high stress drop events is gathered to calculate their median, which could be the cause of the continuous increase in the median stress drop that would otherwise be more abrupt. At about 21°–21.5°S the ID seismicity band is partitioned into a northern and a southern part. At this latitude range the subduction geometry appears significantly perturbed (Sippl et al., 2018) possibly inducing additional zones of increased stress. Interestingly, we observe laterally increased median stress drop in this area (between 21° and 22°S, cf. Figure 10). If higher plate deformation is indeed a significant driver behind the stress drop increase, one could also suspect that it is responsible for the relative maxima of the median stress drop depth variability at shallower depths.

The depth region of 100–140 km also includes by far the greatest amount of earthquakes in the IPOC catalog, especially between 20°S and 22°S. The initially at shallower depths observed parallel bands of seismicity dissolve at 80–100 km depth into a 25–30 km single band of very high activity reaching further down. In addition to the above-mentioned bending, Sippl et al. (2019) discuss the spatial coincidence of the vanishing velocity contrast between oceanic crust and underlying mantle in receiver function studies and the transition of the cold nose to the hot part of the mantle wedge indicated by seismic attenuation images. To explain the strongly increased earthquake productivity, they propose the sudden activation of a kinetically delayed metamorphic reaction with negative volumetric component, which further strengthens the local stress level already in place due to the strong slab pull. The increased observed median stress drops in this area might be an expression of the same process which is responsible for the strong increase in seismic activity in this region.

Seismic coupling can be directly compared to the obtained stress drop distribution along the interface. For example, a very low stress drop region is observed between the rupture patches of the Iquique event and the Tocopilla event (cf. Figure 10) called the *Loa* section of the northern Chilean Margin. One might expect a correlation with low coupling in the same region, but in contrast, several GPS studies find a high coupling (e.g., Hoffmann et al., 2018; Li et al., 2015; Schurr et al., 2014). It is a debated question why neither the Tocopilla earthquake nor the Iquique earthquake have activated this section of the megathrust. One possible explanation might be a creeping behavior, mitigating the potential for large rupture. In California Allmann and Shearer (2007) have reported low stress drop values in the creeping section of the San Andreas fault to the north of the Parkfield event. Their creeping section, however, is separated by a relatively high stress drop barrier from the locked region. Our stress drop map fits into this picture if we consider the few high stress drop values just south of the Iquique large aftershock slip area as indicative for some kind of such barrier. This is supported by observations of repeating earthquakes at that point (Folesky et al., 2022; Soto et al., 2019) which are generally interpreted as indicative for surrounding or adjacent fault creep. Hence, south of the barrier the interface would be considered creeping, also indicated by the relative seismic quiescence, there (Sippl et al., 2023). Further south we observe very low stress drop events which increase in average values until they reach the Tocopilla slip area. From gravity data, a locked asperity hosting potential for a large event generally is correlated with decreased values in the residual gravity field (Wells et al., 2003). In contrast to the prior mentioned locking studies, Bassett and Watts (2015) report a gravity high for this region, which would rather support the interpretation as a creeping segment.

## 6. Conclusions

In this study, we have computed a comprehensive, consistently processed stress drop catalog for Northern Chile. The database for this work is the IPOC catalog, with over 182,000 events in the time period from 2007 to 2021. We additionally perform template matching using the entire waveform archive to obtain an enlarged set of empirical Green's functions. Stress drops are computed by two different methods. First, a spectral ratio approach (SR), which was recently tested in the Iquique earthquake region, is now applied to the entire northern Chile seismic data providing 4,223 stress drops estimates. While these results show already distinct stress drop patterns for some regions, they are limited by the irregular availability of EGFs. To overcome this restriction and to complement the SR results, we second use a modified spectral decomposition approach (SDC). We carefully test and

then apply a modification of the standard SDC technique by using multiple well-defined cells to account for the variability of seismic attenuation in the subduction zone. The SDC approach yields 51,510 stress drop estimates, improving significantly the continuity and coverage of the stress drop catalog. We find a linear relation of the estimated corner frequencies between both approaches,  $f_{c\_SDC} = 0.75 \times f_{c\_SR}$ , translating into  $\Delta\sigma_{SDC} = 0.42 \times \Delta\sigma_{SR}$  for stress drops. Besides the systematic differences in absolute stress drop values, which has also been reported previously in other studies, the two methods produce very similar features.

The SDC-based stress drop distribution represents the first coherent and large-scale stress drop mapping of a subduction zone, including several tens of thousands events. We observe small, but systematic differences of median stress drop values between the seismotectonic domains. Interface seismicity is characterized by the lowest median stress drop of 1.4 MPa. Also, the two slab-parallel seismicity bands within the subducting Nazca plate exhibit rather low median stress drop values of 1.7 and 2.1 MPa, respectively. Upper plate events, which occur almost exclusively in the continental crust, show higher stress drops with a median of 3.3 MPa for the SDC method and 4.0 MPa when using the SR method. Intermediate depth seismicity is monitored down to a depth of about 180 km. It shows a median stress drop of 2.3 MPa. Two additional classes are treated separately in the analysis. For mining induced events, we find particularly small stress drops of about 0.3 MPa. The events from the NN class are poorly constrained; they have the largest location uncertainties and they show heterogeneous stress drops.

Both interface seismicity and the two seismicity bands in the down going slab show only small variations of less than 1 MPa with depth in the interval at 0–80 km depth, that is, the variability of the median stress drop along the subduction is low. Starting at 80 km depth, and especially also for the intermediate depth earthquakes, we observe a consistent increase of the stress drop from about 2 to 15 MPa.

The driving parameter for this increase is the rise of corner frequency with depth, consistently observed from SDC and SR processing. As an explanation for the temporally elevated median stress drop that we observe in proximity of the large megathrust events in the region, we have identified the increased seismic moment release during the fore- and aftershock series.

## Data Availability Statement

Waveform data used in this study were recorded by the seismological CX-net of the Integrated Plate boundary Observatory Chile (IPOC, 2006) using STS-2 broadband seismometers. It was obtained from the EIDA/GEOPHONE web page ([eida.gfz-potsdam.de/webdc3/](http://eida.gfz-potsdam.de/webdc3/) or [geofon.gfz-potsdam.de/waveform/](http://geofon.gfz-potsdam.de/waveform/)). Picks, magnitudes and event hypocenter were taken from Sippl et al. (2023). Data processing and figure production were mainly performed using Python3.5.1 ([python.org](http://python.org)) and packages IPython4.2.0 (Pérez & Granger, 2007), NumPy (Walt et al., 2011), Matplotlib (Hunter, 2007), ObsPy (Beyreuther et al., 2010) and SciPy (Virtanen et al., 2020). Some figures were refined using Inkscape ([inkscape.org](http://inkscape.org)). Results from this study are summarized in a table described and made available in the electronic supplement. They will be permanently stored and openly accessible at <https://zenodo.org/records/10400960>.

## References

- Abercrombie, R. E. (1995). Earthquake source scaling relationships from - 1 to 5 ML using seismograms recorded at 2.5 km depth. *Journal of Geophysical Research*, 100(B12), 24015–24036. <https://doi.org/10.1029/95jb02397>
- Abercrombie, R. E. (2014). Stress drops of repeating earthquakes on the San Andreas Fault at Parkfield. *Geophysical Research Letters*, 41(24), 8784–8791. <https://doi.org/10.1002/2014gl062079>
- Abercrombie, R. E. (2015). Investigating uncertainties in empirical Green's function analysis of earthquake source parameters. *Journal of Geophysical Research: Solid Earth*, 120(6), 4263–4277. <https://doi.org/10.1002/2015jb011984>
- Abercrombie, R. E., Trugman, D. T., Shearer, P. M., Chen, X., Zhang, J., Pennington, C. N., et al. (2021). Does earthquake stress drop increase with depth in the crust? *Journal of Geophysical Research: Solid Earth*, 126(10), e2021JB022314. <https://doi.org/10.1029/2021jb022314>
- Aki, K. (1967). Scaling law of seismic spectrum. *Journal of Geophysical Research*, 72(4), 1217–1231. <https://doi.org/10.1029/jz072i004p01217>
- Allmann, B. P., & Shearer, P. M. (2007). Spatial and temporal stress drop variations in small earthquakes near Parkfield, California. *Journal of Geophysical Research*, 112(B4), B04305. <https://doi.org/10.1029/2006jb004395>
- Allmann, B. P., & Shearer, P. M. (2009). Global variations of stress drop for moderate to large earthquakes. *Journal of Geophysical Research*, 114(B1), B01310. <https://doi.org/10.1029/2008jb005821>
- Bassett, D., & Watts, A. B. (2015). Gravity anomalies, crustal structure, and seismicity at subduction zones: 2. Interrelationships between fore-arc structure and seismogenic behavior. *Geochemistry, Geophysics, Geosystems*, 16(5), 1541–1576. <https://doi.org/10.1002/2014gc005685>
- Beyreuther, M., Barsch, R., Krischer, L., Megies, T., Behr, Y., & Wassermann, J. (2010). ObsPy: A Python toolbox for seismology. *Seismological Research Letters*, 81(3), 530–533. <https://doi.org/10.1785/gssrl.81.3.530>

## Acknowledgments

JF was funded by the German Science Foundation, DFG, project number FO 1325/2-1. This work was performed under the auspices of the U.S. Department of Energy by Lawrence Livermore National Laboratory under Contract DE-AC52-07NA27344. We are grateful to the developers and communities of the utilized open-source resources (cf. D&R section) and we thank all institutions that are involved with operating the IPOC network. We thank the editor Satoshi Ide, the associate editor, reviewer Thomas Goebel and an anonymous reviewer for their constructive comments. Open Access funding enabled and organized by Projekt DEAL.

- Bianchi, M., Evans, P. L., Heinloo, A., & Quinteros, J. (2015). *Webdc3 web interface*. GFZ Data Services. <https://doi.org/10.5880/GFZ.2.4/2016.001>
- Bindi, D., Spallarossa, D., Picozzi, M., & Morasca, P. (2020). Reliability of source parameters for small events in central Italy: Insights from spectral decomposition analysis applied to both synthetic and real data. *Bulletin of the Seismological Society of America*, 110(6), 3139–3157. <https://doi.org/10.1785/0120200126>
- Bloch, W., Kummerow, J., Salazar, P., Wigger, P., & Shapiro, S. (2014). High-resolution image of the North Chilean subduction zone: Seismicity, reflectivity and fluids. *Geophysical Journal International*, 197(3), 1744–1749. <https://doi.org/10.1093/gji/ggu084>
- Boatwright, J. (1980). A spectral theory for circular seismic sources; Simple estimates of source dimension, dynamic stress drop, and radiated seismic energy. *Bulletin of the Seismological Society of America*, 70(1), 1–27.
- Boyd, O. S., McNamara, D. E., Hartzell, S., & Choy, G. (2017). Influence of lithostatic stress on earthquake stress drops in North America. *Bulletin of the Seismological Society of America*, 107(2), 856–868. <https://doi.org/10.1785/0120160219>
- Brune, J. N. (1970). Tectonic stress and the spectra of seismic shear waves from earthquakes. *Journal of Geophysical Research*, 75(26), 4997–5009. <https://doi.org/10.1029/JB075i026p04997>
- Cabrera, L., Ruiz, S., Poli, P., Contreras-Reyes, E., Osses, A., & Mancini, R. (2021). Northern Chile intermediate-depth earthquakes controlled by plate hydration. *Geophysical Journal International*, 226(1), 78–90. <https://doi.org/10.1093/gji/ggaa565>
- Calderoni, G., Rovelli, A., & Singh, S. K. (2013). Stress drop and source scaling of the 2009 April L'Aquila earthquakes. *Geophysical Journal International*, 192(1), 260–274. <https://doi.org/10.1093/gji/ggs011>
- Cesca, S., Grigoli, F., Heimann, S., Dahm, T., Kriegerowski, M., Sobiesiak, M., et al. (2016). The Mw 8.1 2014 Iquique, Chile, seismic sequence: A tale of foreshocks and aftershocks. *Geophysical Journal International*, 204(3), 1766–1780. <https://doi.org/10.1093/gji/ggv544>
- Chen, X., & Abercrombie, R. (2020). Improved approach for stress drop estimation and its application to an induced earthquake sequence in Oklahoma. *Geophysical Journal International*, 223(1), 233–253. <https://doi.org/10.1093/gji/ggaa316>
- Derode, B., & Campos, J. (2019). Energy budget of intermediate-depth earthquakes in northern Chile: Comparison with shallow earthquakes and implications of rupture velocity models used. *Geophysical Research Letters*, 46(5), 2484–2493. <https://doi.org/10.1029/2018gl080962>
- Eshelby, J. D. (1957). The determination of the elastic field of an ellipsoidal inclusion, and related problems. In *Proceedings of the royal society of London a: Mathematical, physical and engineering sciences* (Vol. 241, pp. 376–396).
- Folesky, J., Hofman, R., & Kummerow, J. (2022). On repeating earthquakes in the northern Chilean subduction zone. In *EGU general assembly conference abstracts* (EGU22-7316).
- Folesky, J., Kummerow, J., & Shapiro, S. A. (2018). Patterns of rupture directivity of subduction zone earthquakes in northern Chile. *Journal of Geophysical Research: Solid Earth*, 123(12), 10–785. <https://doi.org/10.1029/2018jb016331>
- Folesky, J., Kummerow, J., & Shapiro, S. A. (2021). Stress drop variations in the region of the 2014  $M_w$  8.1 Iquique earthquake, northern Chile. *Journal of Geophysical Research: Solid Earth*, 126(4), e2020JB020112. <https://doi.org/10.1029/2020jb020112>
- Fuenzalida, A., Schurr, B., Lancieri, M., Sobiesiak, M., & Madariaga, R. (2013). High-resolution relocation and mechanism of aftershocks of the 2007 Tocopilla (Chile) earthquake. *Geophysical Journal International*, 194(2), 1216–1228. <https://doi.org/10.1093/gji/ggt163>
- Goertz-Allmann, B. P., Goertz, A., & Wiemer, S. (2011). Stress drop variations of induced earthquakes at the Basel geothermal site. *Geophysical Research Letters*, 38(9), L09308. <https://doi.org/10.1029/2011gl047498>
- Hardebeck, J. L., & Aron, A. (2009). Earthquake stress drops and inferred fault strength on the Hayward fault, east San Francisco Bay, California. *Bulletin of the Seismological Society of America*, 99(3), 1801–1814. <https://doi.org/10.1785/0120080242>
- Hayes, G. P., Moore, G. L., Portner, D. E., Hearne, M., Flamme, H., Furtney, M., & Smoczyk, G. M. (2018). Slab2, a comprehensive subduction zone geometry model. *Science*, 362(6410), 58–61. <https://doi.org/10.1126/science.aat4723>
- Hoffmann, F., Metzger, S., Moreno, M., Deng, Z., Sippl, C., Ortega-Culaciati, F., & Oncken, O. (2018). Characterizing afterslip and ground displacement rate increase following the 2014 Iquique-Pisagua Mw 8.1 earthquake, Northern Chile. *Journal of Geophysical Research: Solid Earth*, 123(5), 4171–4192. <https://doi.org/10.1002/2017jb014970>
- Hunter, J. D. (2007). Matplotlib: A 2D graphics environment. *Computing in Science & Engineering*, 9(3), 90–95. <https://doi.org/10.1109/mcse.2007.55>
- Hutchings, L., & Viegas, G. (2012). Application of empirical Green's functions in earthquake source, wave propagation and strong ground motion studies. In *Earthquake research and analysis-new frontiers in seismology*. InTech.
- Ide, S., & Beroza, G. C. (2001). Does apparent stress vary with earthquake size? *Geophysical Research Letters*, 28(17), 3349–3352. <https://doi.org/10.1029/2001gl013106>
- IPOC. (2006). IPOC seismic network. Integrated Plate boundary observatory Chile - IPOC [Dataset]. GFZ German Research Centre for Geosciences; Institut des Sciences de l'Univers-Centre National de la Recherche CNRS-INSU, Seismic Network (Vol. Seismic Network). <https://doi.org/10.14470/PK615318>
- Ji, C., Archuleta, R. J., & Wang, Y. (2022). Variability of spectral estimates of stress drop reconciled by radiated energy. *Bulletin of the Seismological Society of America*, 112(4), 1871–1885. <https://doi.org/10.1785/0120210321>
- Kanamori, H., & Anderson, D. L. (1975). Theoretical basis of some empirical relations in seismology. *Bulletin of the Seismological Society of America*, 65, 1073–1095.
- Kaneko, Y., & Shearer, P. M. (2014). Seismic source spectra and estimated stress drop derived from cohesive-zone models of circular subshear rupture. *Geophysical Journal International*, 197(2), 1002–1015. <https://doi.org/10.1093/gji/ggu030>
- Kaneko, Y., & Shearer, P. M. (2015). Variability of seismic source spectra, estimated stress drop, and radiated energy, derived from cohesive-zone models of symmetrical and asymmetrical circular and elliptical ruptures. *Journal of Geophysical Research: Solid Earth*, 120(2), 1053–1079. <https://doi.org/10.1002/2014JB011642>
- Li, S., Moreno, M., Bedford, J., Rosenau, M., & Oncken, O. (2015). Revisiting viscoelastic effects on interseismic deformation and locking degree: A case study of the Peru-North Chile subduction zone. *Journal of Geophysical Research: Solid Earth*, 120(6), 4522–4538. <https://doi.org/10.1002/2015jb011903>
- Madariaga, R. (1976). Dynamics of an expanding circular fault. *Bulletin of the Seismological Society of America*, 66(3), 639–666. <https://doi.org/10.1785/bssa0660030639>
- Münchmeyer, J., Bindi, D., Sippl, C., Leser, U., & Tilmann, F. (2020). Low uncertainty multifeature magnitude estimation with 3-D corrections and boosting tree regression: Application to North Chile. *Geophysical Journal International*, 220(1), 142–159. <https://doi.org/10.1093/gji/ggz416>
- Neely, J. S., Stein, S., & Spencer, B. D. (2020). Large uncertainties in earthquake stress-drop estimates and their tectonic consequences. *Seismological Research Letters*, 91(4), 2320–2329. <https://doi.org/10.1785/0220200004>
- Nishitsuji, Y., & Mori, J. (2014). Source parameters and radiation efficiency for intermediate-depth earthquakes in northeast Japan. *Geophysical Journal International*, 196(2), 1247–1259. <https://doi.org/10.1093/gji/ggt458>

- Patzwahl, R., Mechie, J., Schulze, A., & Giese, P. (1999). Two-dimensional velocity models of the Nazca plate subduction zone between 19.5 S and 25 S from wide-angle seismic measurements during the CINCA95 project. *Journal of Geophysical Research*, *104*(B4), 7293–7317. <https://doi.org/10.1029/1999jb900008>
- Pennington, C. N., Chen, X., Abercrombie, R. E., & Wu, Q. (2021). Cross validation of stress drop estimates and interpretations for the 2011 Prague, ok, earthquake sequence using multiple methods. *Journal of Geophysical Research: Solid Earth*, *126*(3), e2020JB020888. <https://doi.org/10.1029/2020jb020888>
- Pérez, F., & Granger, B. E. (2007). IPython: A system for interactive scientific computing. *Computing in Science & Engineering*, *9*(3), 21–29. <https://doi.org/10.1109/mcse.2007.53>
- Poli, P., & Prieto, G. A. (2016). Global rupture parameters for deep and intermediate-depth earthquakes. *Journal of Geophysical Research: Solid Earth*, *121*(12), 8871–8887. <https://doi.org/10.1002/2016jb013521>
- Prieto, G. A., Florez, M., Barrett, S. A., Beroza, G. C., Pedraza, P., Blanco, J. F., & Poveda, E. (2013). Seismic evidence for thermal runaway during intermediate-depth earthquake rupture. *Geophysical Research Letters*, *40*(23), 6064–6068. <https://doi.org/10.1002/2013gl058109>
- Prieto, G. A., Shearer, P. M., Vernon, F. L., & Kilb, D. (2004). Earthquake source scaling and self-similarity estimation from stacking P and S spectra. *Journal of Geophysical Research*, *109*(B8), B08310. <https://doi.org/10.1029/2004jb003084>
- Ruiz, S., Metois, M., Fuenzalida, A., Ruiz, J., Leyton, F., Grandin, R., et al. (2014). Intense foreshocks and a slow slip event preceded the 2014 Iquique Mw 8.1 earthquake. *Science*, *345*(6201), 1165–1169. <https://doi.org/10.1126/science.1256074>
- Schurr, B., Asch, G., Hainzl, S., Bedford, J., Hoehner, A., Palo, M., et al. (2014). Gradual unlocking of plate boundary controlled initiation of the 2014 Iquique earthquake. *Nature*, *512*(7514), 299–302. <https://doi.org/10.1038/nature13681>
- Schurr, B., Asch, G., Rosenau, M., Wang, R., Oncken, O., Barrientos, S., et al. (2012). The 2007  $M_{7.7}$  Tocopilla northern Chile earthquake sequence: Implications for along-strike and downdip rupture segmentation and megathrust frictional behavior. *Journal of Geophysical Research*, *117*(B5), B05305. <https://doi.org/10.1029/2011jb009030>
- Schurr, B., Moreno, M., Tréhu, A. M., Bedford, J., Kummerow, J., Li, S., & Oncken, O. (2020). Forming a Mogi doughnut in the years prior to and immediately before the 2014  $M_{8.1}$  Iquique, northern Chile, earthquake. *Geophysical Research Letters*, *47*(16), e2020GL088351. <https://doi.org/10.1029/2020gl088351>
- Sen, A. T., Cesca, S., Lange, D., Dahm, T., Tilmann, F., & Heimann, S. (2015). Systematic changes of earthquake rupture with depth: A case study from the 2010  $M_w$  8.8 Maule, Chile, earthquake aftershock sequence systematic changes of earthquake rupture with depth. *Bulletin of the Seismological Society of America*, *105*(5), 2468–2479. <https://doi.org/10.1785/0120140123>
- Shaw, B. E. (2009). Constant stress drop from small to great earthquakes in magnitude-area scaling. *Bulletin of the Seismological Society of America*, *99*(2A), 871–875. <https://doi.org/10.1785/0120080006>
- Shearer, P. M., Abercrombie, R. E., Trugman, D. T., & Wang, W. (2019). Comparing EGF methods for estimating corner frequency and stress drop from P wave spectra. *Journal of Geophysical Research: Solid Earth*, *124*(4), 3966–3986. <https://doi.org/10.1029/2018jb016957>
- Shearer, P. M., Prieto, G. A., & Hauksson, E. (2006). Comprehensive analysis of earthquake source spectra in southern California. *Journal of Geophysical Research*, *111*(B6), B06303. <https://doi.org/10.1029/2005jb003979>
- Sippl, C., Dielforder, A., John, T., & Schmalholz, S. M. (2022). Global constraints on intermediate-depth intraslab stresses from slab geometries and mechanisms of double seismic zone earthquakes. *Geochemistry, Geophysics, Geosystems*, *23*(9), e2022GC010498. <https://doi.org/10.1029/2022gc010498>
- Sippl, C., Schurr, B., Asch, G., & Kummerow, J. (2018). Seismicity structure of the Northern Chile forearc from > 100,000 double-difference relocated hypocenters. *Journal of Geophysical Research: Solid Earth*, *123*(5), 4063–4087. <https://doi.org/10.1002/2017JB015384>
- Sippl, C., Schurr, B., John, T., & Hainzl, S. (2019). Filling the gap in a double seismic zone: Intraslab seismicity in Northern Chile. *Lithos*, *346*, 105155. <https://doi.org/10.1016/j.lithos.2019.105155>
- Sippl, C., Schurr, B., Münchmeyer, J., Barrientos, S., & Oncken, O. (2023). The Northern Chile forearc constrained by 15 years of permanent seismic monitoring. *Journal of South American Earth Sciences*, *126*, 104326. <https://doi.org/10.1016/j.jsames.2023.104326>
- Soto, H., Sippl, C., Schurr, B., Kummerow, J., Asch, G., Tilmann, F., et al. (2019). Probing the Northern Chile megathrust with seismicity: The 2014  $M_{8.1}$  Iquique earthquake sequence. *Journal of Geophysical Research: Solid Earth*, *124*(12), 12935–12954. <https://doi.org/10.1029/2019jb017794>
- Tian, D., Wei, S. S., Wang, W., & Wang, F. (2022). Stress drops of intermediate-depth and deep earthquakes in the Tonga slab. *Journal of Geophysical Research: Solid Earth*, *127*(10), e2022JB025109. <https://doi.org/10.1029/2022jb025109>
- Trugman, D. T. (2020). *Stress-drop and source scaling of the 2019 Ridgecrest, California, earthquake sequence*. Bulletin of the Seismological Society of America.
- Trugman, D. T., & Shearer, P. M. (2017). Application of an improved spectral decomposition method to examine earthquake source scaling in Southern California. *Journal of Geophysical Research: Solid Earth*, *122*(4), 2890–2910. <https://doi.org/10.1002/2017jb013971>
- Uchide, T., Shearer, P. M., & Imanishi, K. (2014). Stress drop variations among small earthquakes before the 2011 Tohoku-Oki, Japan, earthquake and implications for the main shock. *Journal of Geophysical Research: Solid Earth*, *119*(9), 7164–7174. <https://doi.org/10.1002/2014jb010943>
- Viegas, G., Abercrombie, R. E., & Kim, W.-Y. (2010). The 2002  $M_5$  au sable forks, NY, earthquake sequence: Source scaling relationships and energy budget. *Journal of Geophysical Research*, *115*(B7), B07310. <https://doi.org/10.1029/2009jb006799>
- Virtanen, P., Gommers, R., Oliphant, T. E., Haberland, M., Reddy, T., Cournapeau, D., et al. (2020). Scipy 1.0: Fundamental algorithms for scientific computing in Python. *Nature Methods*, *17*(3), 1–12. <https://doi.org/10.1038/s41592-019-0686-2>
- Walt, S. V. D., Colbert, S. C., & Varoquaux, G. (2011). The NumPy array: A structure for efficient numerical computation. *Computing in Science & Engineering*, *13*(2), 22–30. <https://doi.org/10.1109/mcse.2011.37>
- Wells, R. E., Blakely, R. J., Sugiyama, Y., Scholl, D. W., & Dinterman, P. A. (2003). Basin-centered asperities in great subduction zone earthquakes: A link between slip, subsidence, and subduction erosion? *Journal of Geophysical Research*, *108*(B10), 2507. <https://doi.org/10.1029/2002jb002072>
- Ye, L., Lay, T., Kanamori, H., & Rivera, L. (2016). Rupture characteristics of major and great ( $M_w \geq 7.0$ ) megathrust earthquakes from 1990 to 2015: 1. Source parameter scaling relationships. *Journal of Geophysical Research: Solid Earth*, *121*(2), 826–844. <https://doi.org/10.1002/2015jb012426>